

# Low Velocity Impact of Flat and Doubly Curved Polycarbonate Panels

**G. O. Antoine**

Department of Biomedical Engineering and  
Mechanics (M/C 0219),  
Virginia Polytechnic Institute and  
State University,  
Blacksburg, VA 24061  
e-mail: antoineg@vt.edu

**R. C. Batra<sup>1</sup>**

Fellow ASME  
Department of Biomedical  
Engineering and Mechanics (M/C 0219),  
Virginia Polytechnic Institute and  
State University,  
Blacksburg, VA 24061  
e-mail: rbatra@vt.edu

*Three-dimensional finite transient deformations of polycarbonate (PC) panels impacted at low velocity by a hemispherical-nosed rigid cylinder have been studied by using the commercial finite element software LS-DYNA with a thermo-elasto-viscoplastic material model for the PC incorporated in it as a user defined subroutine. The implementation of the subroutine has been verified by comparing analytical and numerical solutions of simple initial-boundary-value problems. The mathematical model of the low velocity impact problem has been validated by comparing the computed and the experimental results for the maximum deflection and time histories of the centroidal deflection. It is found that the initial slope of the reaction force between the impactor and the panel versus the indentation for a curved panel can be nearly 20 times that for the flat panel of the same thickness as the curved panel. For the impact velocities considered, it is found that the maximum effective plastic strain in the PC shell near the center of impact and the dominant deformation mode there strongly depend on the panel curvature, the panel thickness, and the impact speed. Effects of the panel curvature, the panel thickness, and the impact speed on stresses and strains developed in a panel are delineated. This information should help designers of impact resistant transparent panels such as an airplane canopy, automobile windshield, and goggles. However, damage initiation and propagation, and the final indentation induced in the clamped panels have not been computed.*

[DOI: 10.1115/1.4029779]

*Keywords:* impact, flat and curved panels, finite element analysis, thermo-elasto-viscoplastic material

## 1 Introduction

Polymers are composed of long chains of monomers while a metal is generally a polycrystalline material. This difference in the microstructure usually influences their thermomechanical response to applied loads. Polymers usually exhibit strong strain-rate dependence and are widely used as transparent armor because of their high specific impact resistance, e.g., see Ref. [1]. Sands et al. [2] have reported that PCs have better specific impact resistance than most glasses. A lightweight transparent PC panel is subjected to low velocity impact when either a stone hits a windshield of a car or when police use curved panels to protect themselves from rocks thrown at them by a crowd of people during riots. Mathematical and computational models that can reliably predict the response of these panels to low velocity impact will help improve upon their design and possibly reduce their weight.

Deformations of PC have been experimentally studied at different strain rates and temperatures in uniaxial compression/tension and simple shear [3–11]. The test results have demonstrated that a PC material initially deforms elastically and exhibits strain softening subsequent to yielding that is followed by strain hardening at large strains. Moreover, increasing the temperature decreases the yield stress and increases the yield strain of the PC, while increasing the strain rate has the opposite effect. Young's modulus (initial elastic modulus) of the material increases with an increase in the strain rate but decreases with a rise in the temperature. Furthermore, the PC material can undergo large plastic deformations before failure. The energy dissipated due to plastic

deformations is partially converted into heat for low [12,13] and high strain rates [14]. For high strain-rate deformations of PC samples, and assuming adiabatic heating of the material, Rittel [14] introduced two parameters  $\beta_{\text{diff}}$  and  $\beta_{\text{int}}$  relating the rate of heating to the plastic working, and the accumulated heating to the total plastic work, respectively. He found that for strain rates greater than 5000/s,  $\beta_{\text{int}}$  varies between 0.4 and 1, while  $\beta_{\text{diff}}$  can be 2.5 (larger than 1), which he attributed to the conversion of the elastic energy into heat during the softening regime.

Different constitutive equations (or material models) for the mechanical response of the PC have been proposed [5,15–17]. They usually simulate the nonlinear elastic response of the PC with a Langevin spring and the elasto-viscoplastic response by using spring-dashpot systems modified to account for large deformations. Here, we adopt the phenomenological model developed by Mulliken and Boyce [5] and modified by Varghese and Batra [18,19] to account for effects of temperature rise due to adiabatic heating and strain- and strain-rate hardening. Thus, material response depends upon the strain rate and the temperature. We note that the Mulliken and Boyce [5] model was recently extended to very high strain rates ( $>10^4$ /s) by Safari et al. [20]. However, this extension is not included here because we learned of it after having completed most of the work, and strain rates anticipated to occur in the PC plate at low velocity impact are expected to be considerably less than  $10^4$ /s. Moreover, damage evolution and failure criterion have not been considered for the impact problems studied herein mainly because these are not included in the user defined subroutine we have implemented in LS-DYNA. However, we investigate coupled thermomechanical deformations of monolithic PC panels of different thicknesses, curvatures, and for different impact speeds.

The effect of curvature on the impact response of laminates has been studied both experimentally [21,22] and numerically [23–28]. It is found that the curvature of sandwich panels changes

<sup>1</sup>Corresponding author.

Contributed by the Applied Mechanics Division of ASME for publication in the JOURNAL OF APPLIED MECHANICS. Manuscript received November 10, 2014; final manuscript received February 7, 2015; published online February 26, 2015. Assoc. Editor: Weinong Chen.

the deformation regimes (bending becomes more important for curved panels) [21] and decreases their blast resistance [22] because the larger area of deformation of flat plates enables them to absorb more energy. In Refs. [24,25], a semi-analytical approach is used to analyze deformations of curved graphite–epoxy laminates. It is found that the curvature degrades the impact performance of the laminate, since with an increase in the shell curvature [24] the maximum in-plane strain induced at the shell centroid and the peak contact force between the impactor and the laminate increase [25]. Transient deformations of curved linear elastic composite panels have been analyzed by the finite element method (FEM) in Refs. [23,26–28]. Results presented in Ref. [26] suggest that the curvature does not significantly change the time history of the contact force between the plate/shell and the impactor; in particular the maximum contact force is the same for the flat plate and the singly and the doubly curved panels. However, other works report that the shell curvature increases the maximum contact force due to the enhanced bending stiffness of curved panels [23,25,27,28]. The apparent contradiction regarding the dependence of the peak contact force upon the shell curvature is possibly due to different materials, geometries, and loadings considered in these papers. Thus, the effect of shell curvature on deformations induced in flat and curved panels is not well understood. Numerical studies cited above have assumed the plate material to be linear elastic. However, most materials including composites have nonlinear stress–strain curves. Here, we consider material and geometric nonlinearities as well as the effect of negative curvature not heretofore studied. By negative (positive) curvature, we mean that the center of curvature and the impactor are located on the same (opposite) side of the panel.

The objectives of the study are to determine the effects of the panel curvature, the impact speed, and the panel thickness on the contact force between the impactor and panels, and on stresses, strains, and plastic deformations developed in the panel. A major difference between the current work and most works summarized above is that the PC material can undergo large plastic deformations whereas the glass/epoxy composites studied in the above cited works fail at very small strains.

The rest of the paper is organized as follows. We formulate the initial-boundary-value problem in Sec. 2 and describe the corresponding computational model in Sec. 3. The constitutive relation for the PC is briefly described in Appendix A. Results for the low velocity impact of flat and curved panels and their comparisons with the test data available in the literature are presented and discussed in Sec. 4. Conclusions from this work are summarized in Sec. 5.

## 2 Mathematical Model

A schematic sketch of the problem studied is exhibited in Fig. 1. Either a flat or a curved monolithic panel of sides  $L_1$  and  $L_2$  and thickness  $h$  clamped on all four edges is impacted at normal incidence by a steel cylinder with a hemispherical nose of diameter  $d$ . We describe deformations of the panel by using

rectangular Cartesian coordinate axes with the origin at the centroid of the top face of the panel, the positive  $x$ -axis pointing to the right, and the positive  $z$ -axis pointing upward.

In the Lagrangian description of motion, transient deformations of the panel are governed by the following conservation laws:

$$\begin{aligned} \text{mass :} & \quad \rho J = \rho_0 \\ \text{linear momentum :} & \quad \rho_0 \dot{\mathbf{v}} = \hat{\nabla} \cdot \mathbf{T} \\ \text{moment of momentum :} & \quad \mathbf{T} \cdot \mathbf{F}^T = \mathbf{F} \cdot \mathbf{T}^T \\ \text{internal energy :} & \quad \rho_0 c \dot{\theta} = \hat{Q} \end{aligned} \quad (1)$$

Here,  $\rho$  and  $\rho_0$  are mass densities in the current and the reference configurations, respectively,  $c$  is the specific heat,  $J = \det(\mathbf{F})$ ,  $\mathbf{F} = \partial \mathbf{x} / \partial \mathbf{X}$  is the deformation gradient that maps a material point from the reference position  $\mathbf{X}$  to its current location  $\mathbf{x}$ , a superimposed dot indicates the material time derivative,  $\mathbf{v}$  is the velocity of a material point,  $\mathbf{T}$  is the first Piola–Kirchhoff stress tensor related to the Cauchy stress tensor  $\boldsymbol{\sigma}$  by  $\mathbf{T} = J \boldsymbol{\sigma} \cdot \mathbf{F}^{-T}$ ,  $(\hat{\nabla} \cdot)$  is the divergence operator with respect to  $\mathbf{X}$ , and  $\hat{Q}$  is the heating per unit reference volume produced due to viscous and plastic deformations. Deformations are assumed to be locally adiabatic, thus heat conduction is neglected. This is a reasonable assumption since results have been computed only for 5 ms which is not enough time for significant heat transfer to occur due to conduction. This assumption also enables one to use larger time steps during the numerical solution of the problem. However, mechanical and thermal deformations of the PC are coupled since energy dissipation contributes to the temperature rise, and the current temperature affects values of Young’s modulus and the evolution of the effective plastic strain as explained in Appendix A. For impact speeds studied here, deformations of the steel impactor are assumed to be negligible as compared to those of the PC panel and are thus neglected. The impactor is taken to be a rigid hemispherical-nosed cylinder, not exchange heat with the panel, and has only translational motion governed by

$$\dot{\mathbf{p}} = \mathbf{f} \quad (2)$$

where  $\mathbf{p}$  equals the linear momentum and  $\mathbf{f}$  is the resultant force acting on the impactor. For transient problems involving low to moderate impact speeds, Khalili et al. [29] have shown that assuming the impactor to be rigid reduces the computation time with minor effects on numerical results.

At points on a clamped edge, the three displacement components are set equal to zero. At a free surface, the surface tractions vanish. On the smooth contact surface between the impactor and the panel, we apply the following continuity conditions:

$$\begin{aligned} \text{normal velocity :} & \quad [\![\dot{\mathbf{u}}]\!] \cdot \mathbf{n} = 0 \\ \text{normal traction :} & \quad [\![\mathbf{t}]\!] \cdot \mathbf{n} = 0 \\ \text{tangential traction :} & \quad \mathbf{t} \times \mathbf{n} = \mathbf{0} \end{aligned} \quad (3)$$

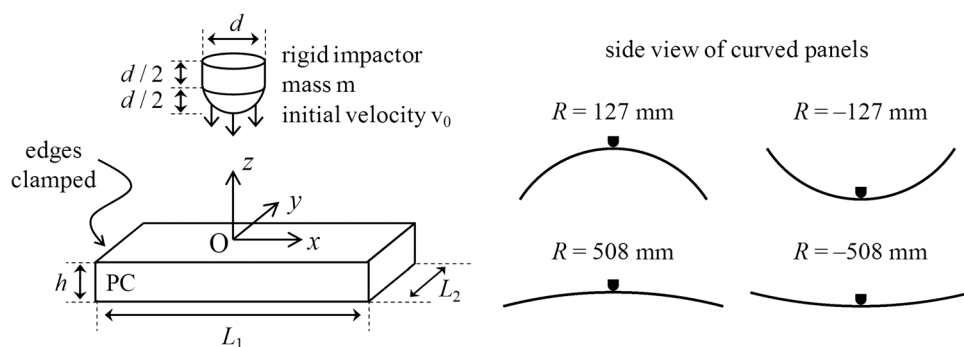


Fig. 1 Sketch of the impact problem studied

Here, double brackets enclosing a variable indicate the jump in its value across the contact surface,  $\mathbf{n}$  is a unit normal to the contact surface,  $\mathbf{u}$  is the displacement field,  $\dot{\mathbf{u}}$  is the velocity field,  $\mathbf{t}$  is the traction vector, and the symbol  $\times$  denotes the cross product between two three-dimensional vectors. These conditions imply that there is no interpenetration between the impactor and the panel. At a point on the contact surface, the normal component of velocity and surface traction is continuous, and the tangential traction vanishes. Because of the assumption of locally adiabatic deformations of the PC, no boundary conditions for the thermal part are needed. Also, no continuity conditions on the temperature and the normal component of the heat flux are required at the interface between the impactor and the panel. This approximation considerably simplifies the problem. Problems with heat exchange between the impactor and the target have been studied, for example, in Ref. [30].

At time  $t = 0$ , the panel is at rest, stress free, at the uniform temperature of 300 K, and the moving impactor just contacts the top surface of the panel.

The thermo-elasto-viscoplastic response of the PC is modeled by the Mulliken and Boyce [5] constitutive relation with the modifications suggested by Varghese and Batra [18]. It is briefly described in Appendix A for easy reference where the expression for  $\dot{Q}$  is also given. When the magnitude of the axial stress is plotted against the magnitude of the axial strain, the stress-strain curves for the PC in uniaxial tension and compression are different, and the initial yield stress (defined here as the maximum value of the effective stress, or the von Mises stress, on the straight line portion of the curves) in tension is smaller than that in compression, see Fig. 2. Thus even in pure bending of a straight beam, deformations of the PC layer will in general be not symmetric about the beam midsurface. For uniaxial deformations, the effective stress equals the axial stress and for simple shear deformations it equals  $\sqrt{3}$  times the shear stress. It is clear from results plotted in Fig. 2 that the response of the PC in simple shearing deformations is close to that in uniaxial tension. For an isotropic metal, the three curves usually overlap. The effective strain here is defined as  $(2\epsilon^T \epsilon^T / 3)^{1/2}$  where  $\epsilon^T$  is the deviatoric Hencky strain tensor. For problems studied here, the effect of degradation of material properties due to damage induced has been ignored. Furthermore, the PC is assumed not to fail.

### 3 Computational Model

We use the commercial FE software LS-DYNA in which the constitutive relation for the PC has been implemented as a user-defined subroutine written in FORTRAN. The verification of the implementation has been described by Varghese and Batra [18].

Khalili et al. [29] have analyzed an impact problem using different shell elements, integration schemes, and FE meshes. They found that an “unstructured” FE mesh gave better convergence rate versus

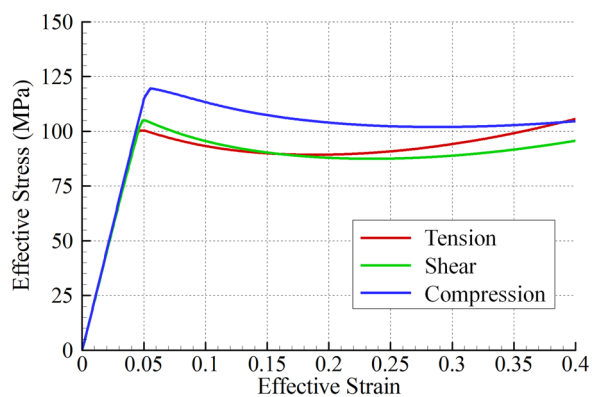


Fig. 2 Effective true stress versus effective true strain for uniaxial tension, simple shear, and uniaxial compression of the PC at 5000/s true strain rate

computational cost than a structured FE mesh. Here, we use a non-uniform FE mesh consisting of eight-node brick elements with one point integration rule for evaluating element matrices and the Belytschko–Bindeman hourglass control algorithm. For a sample problem, the energy of hourglass modes of deformation was found to be less than 5% of the total strain energy of deformations.

We analyzed a quasi-static Hertz contact problem with LS-DYNA by considerably increasing the mass density of the PC to ensure that we were correctly using the code. We studied the indentation by a 50 mm diameter rigid sphere of a 160 mm thick and 500 mm diameter cylindrical linear elastic plate with Young’s modulus  $E = 10$  GPa and Poisson’s ratio  $\nu = 0.25$ , and the mantle and the bottom face clamped. We used as reference the Hertz solution for the contact force between the rigid indenter and a semi-infinite linear elastic half space. For maximum 3 mm indentation, the disk can be regarded as a half space. The analytical and the computed reaction forces as a function of the indentation depth are plotted in Fig. 3. One can see that for indentation depth less than 1 mm, the deviation between the two sets of results is less than 5%. We note that the initial large difference is due to the numerical noise when the contact force is very small.

For each impact problem studied, results were computed with at least two FE meshes. The FE mesh A was uniformly refined to obtain a finer FE mesh B having at least 30% more nodes than those in mesh A. The process was repeated till the maximum reaction force and the energy dissipation computed with the two successive FE meshes differed by less than 10%. We have included in Appendix B a typical FE mesh used in the analysis and how it was generated.

## 4 Results and Discussion

### 4.1 Impact of Flat Plates

4.1.1 *Validation of the Model.* We have simulated test configurations of Gunnarsson et al. [31–33] who used the digital image correlation technique to experimentally measure deflection of the back face of clamped 254 mm square PC plates of thickness varying between 3 and 12.32 mm as they were impacted by a 104 g impactor at speeds ranging from 10 to 50 m/s. In Ref. [33], the authors provide the time history of the deflection of the center of the rear face of 3, 4.45, 5.85, 9.27, and 12.32 mm thick panels, while in Ref. [31] they give deformed profiles of the rear face of the 5.60 mm thick panel. The measured and the computed maximum deflections listed in Table 1 reveal that the largest difference, 10.3%, between them is for the 12.32 mm thick panel impacted at 40 m/s. The impact speeds given in the Table have been rounded off from those listed in Refs. [31–33].

We have exhibited in Fig. 4 the computed and the experimental [33] time histories of the maximum deflections of the 4.45 and the

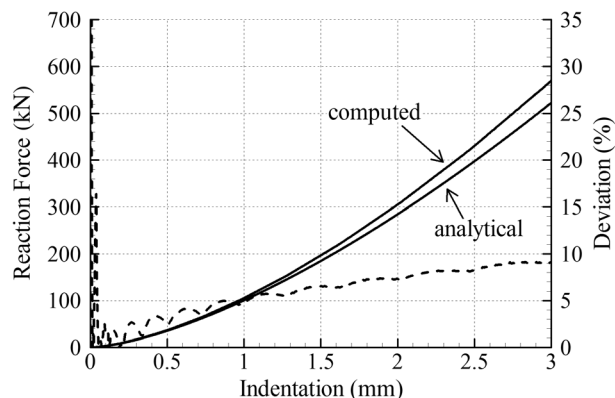


Fig. 3 Analytical and computed reaction forces (solid lines) and the % difference between them (dashed line) as a function of the indentation

**Table 1 Comparison of the experimental [33] and the computed maximum deflections of the centroid of the back surface of clamped PC plates**

Panel thickness (mm)	Approximate impact velocity (m/s)				
	10	20	30	40	50
	Experimental (computed) maximum deflection in mm and % difference between the two values				
3.00	13.2 (13.0) [-1.5]	16.1 (17.1) [6.2]			
4.45	9.4 (9.0) [-4.3]	12.9 (13.1) [1.6]			
5.85	6.5 (7.1) [9.2]	10.9 (10.2) [-6.4]	15.2 (14.8) [-2.6]	19.2 (19.0) [-1.0]	22.0 (22.7) [3.2]
9.27			10.2 (10.4) [2.0]	11.3 (12.1) [7.1]	14.0 (14.8) [5.7]
12.32			6.9 (7.3) [5.8]	8.7 (9.6) [10.3]	10.7 (11.3) [5.6]

12.32 mm thick plates for different impact speeds. The two time histories agree well with each other during the initial rising portion for the five problems studied. For the 12.32 mm thick plate and impact speeds of 30, 40.7, and 48.9 m/s, the computed and the experimental time histories of the maximum deflection are close to each other even when the deflection is decreasing but that is not the case for the 4.45 mm thick panel impacted at 10.5 and 19.1 m/s. In the experimental results for the 12.32 mm thick plate, the maximum deflection occurs at approximately 0.9 ms for the three impact speeds. However, for the 4.45 mm thick panel, the times of the maximum deflection equal 2.5 and 1.5 ms, respectively, for impact speeds of 19.1 and 10.5 m/s. The qualitative features are well captured by the mathematical model. However, the quantitative agreement between the two sets of results is the best for the 4.45 mm thick panel impacted at 19.1 m/s.

We note that for elastic deformations of a flat plate, the bending rigidity is proportional to the (thickness)<sup>3</sup>. For a plate made of an elastic-perfectly plastic material (i.e., the yield stress stays constant), the bending rigidity of a fully plastically deformed cross section is proportional to (thickness)<sup>2</sup> and a plastic hinge forms there. For an elasto-viscoplastic material with different yield stresses in tension and compression, the dependence of the bending rigidity can be a complex function of the plate thickness. One measure of inertia effects is the ratio of the kinetic energy density to the yield stress of the material which does not involve the plate thickness; e.g., see Ref. [34]. Even though we provide below (cf. Fig. 9) details of deformations on a cross section, these have not enabled us to find reasons for the differences between the computed and the experimental time histories of the maximum deflections for the five problems studied. Deformations of the panel are quite complicated with bending and stretching dominant at different portions of a panel. A possibility is to conduct the

sensitivity study similar to that performed in Ref. [35] to delineate parameters to which the maximum deflection is most sensitive.

The experimentally observed and the computed deformed shapes, at different times, of the central portion of the rear face of the 5.60 mm thick panel impacted at 30.5 m/s are shown in Fig. 5. The comparisons between the deformed shapes at the other impact speeds are similar to this one and are not exhibited. The computed maximum deflection at the plate centroid is a little more than the corresponding experimental one for the first three times but a little less for the latter two time instants considered. Overall, the computed deformed shapes are close to the corresponding experimental ones at each one of the five times.

*4.1.2 Effect of Plate Thickness for 30.0 m/s Impact Speed.* We have numerically simulated deformations of 3, 4.45, 5.85, 9.27, and 12.32 mm thick 254 mm square clamped flat plates impacted by the smooth rigid cylinder (mass 104 g, nose radius 6.35 mm) imparting to panels the kinetic energy and the linear momentum of 46.8 J and 3.12 N s, respectively.

In order to ascertain dominant deformation modes in the impacted plates, we define the overall average axial stress at a point  $T_{axial}$  and its through-the-thickness average  $T_{axial,avg}$  by

$$\hat{T}_{axial} = \left[ \left( \frac{\mathbf{F} \cdot \mathbf{N}}{\|\mathbf{F} \cdot \mathbf{N}\|} \right)^T \cdot \mathbf{T} \cdot \mathbf{N} \right], \quad T_{axial} = \frac{1}{t_f} \int_{t=0}^{t_f} \hat{T}_{axial} dt,$$

$$T_{axial,avg} = \frac{1}{h} \int_{Z=-h}^0 T_{axial} dZ \quad (4)$$

Here,  $T_{axial}$  is the axial stress at a point averaged over time from the beginning of impact till the time  $t_f$  when the impactor finally separates from the plate and not the time when the plate comes to

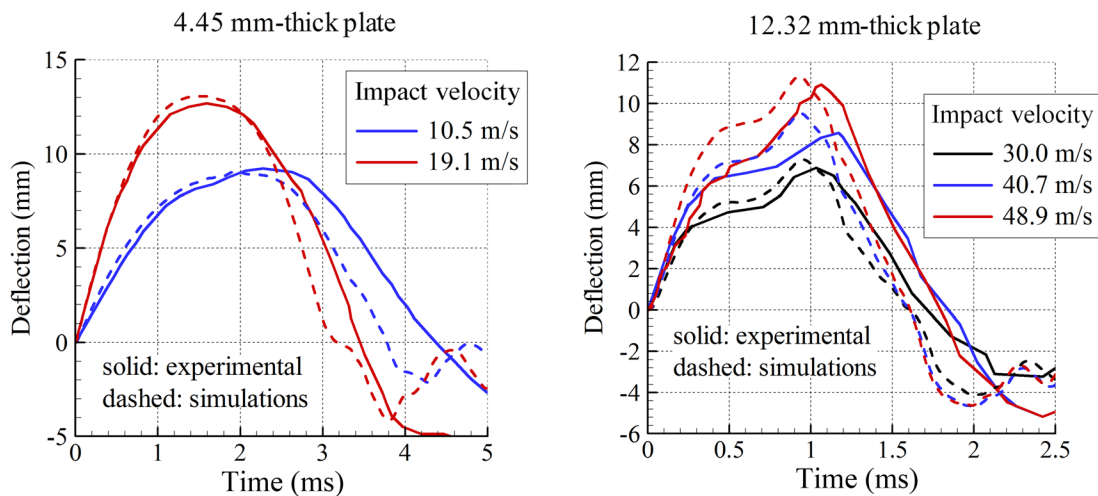


**Fig. 4 Time histories of the deflection (experimental data from Ref. [33]) of the centroid of the back surface of two panels for different impact velocities**

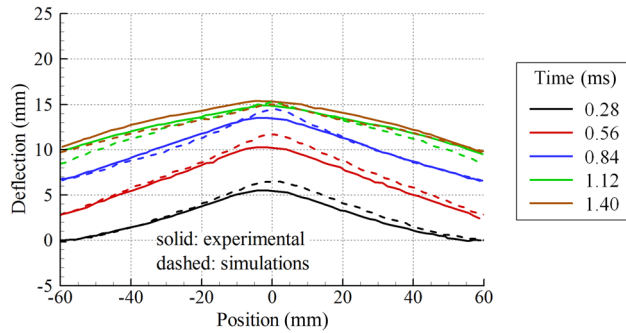


**Fig. 5 Deformed shapes at different times of the back surface of the 5.60 mm thick PC panel impacted at 30.5 m/s. Experimental data from Ref. [31].**

rest, and  $\mathbf{N}$  is a unit vector normal to the local cross section in the undeformed configuration and pointing toward the panel center. Thus, the value of  $t_f$  varies with the plate thickness and the impact speed. Values of  $t_f$  equal 3.02, 2.78, 2.6, 2.1, and 1.74 ms, respectively, for the 3, 4.45, 5.85, 9.27, and 12.32 mm thick plates. That is,  $t_f$  monotonically decreases with an increase in the plate thickness.

The  $T_{axial,avg}$  equals the value of  $T_{axial}$  averaged over a transverse normal to the midsurface of the panel in the reference configuration and is related to the through-the-thickness averaged stretching of the panel. We note that both  $T_{axial}$  and  $T_{axial,avg}$  give the time-averaged values rather than the instantaneous values at a point. The difference between values of  $T_{axial}$  at points of intersection of a transverse normal to the panel midsurface with its top and the bottom surfaces is related to the local bending of the panel; a negative (positive) value of this difference will imply that on the average points on the transverse normal have experienced either bending or compressive (tensile) deformations with the panel locally deformed concave upward (downward). Because of the difference in the yield stress of the PC in tension and compression, the foregoing statement is approximately valid. The variations with the  $x$ -coordinate along the centroidal axis of  $T_{axial,avg}$  and the difference in the values of  $T_{axial}$  at corresponding points on the top and the bottom surfaces are shown in Fig. 6 for the five thickness values. These results evince that in the 3 mm thick plate the average axial stress is tensile and is much higher than that in the thicker plates implying that stretching deformations are dominant in the thin plate. This is further confirmed by the relatively small difference between values of the axial stress on the top and

the bottom surfaces of the plate (cf. Fig. 6 right). In the 9.27 and the 12.32 mm thick plates,  $T_{axial,avg}$  is negative or compressive near the center of impact (cf. Fig. 6 left). It becomes positive at points situated at least 7.5 and 10 mm away from the panel center.

At time  $t_f$ , the central portions of the deformed cross sections of plates and fringe plots of the effective plastic strain are exhibited in Fig. 7. It is clear that deformations of the 3 mm thick plate are quite different from those of the 9.27 and the 12.32 mm thick plates, plastic deformations are highly localized near the impacted point, and the maximum effective plastic strain in the 3 mm thick panel is more than twice of that in the 12.32 mm thick panel. For each plate, strains are not symmetric about the midsurface due to stretching deformations and the difference in the yield stress in tension and compression for the PC. However, the difference in the effective plastic strains is much more than that due to the difference in the yield stresses. Whereas the 12.32 mm thick plate has noticeable plastic strains around the impact point and near the top surface, the other four plates have more plastic deformations in the same general region near the bottom surface. The impactor stays in contact with the 3 and the 4.45 mm thick panels throughout their  $1/2$  cycle of motion, it loses contact for the 5.85, 9.27, and 12.32 mm thick panels before they revert back to the position of zero deflection. The deformed regions of plates under the impactor have larger slopes near the crater edges for the thinnest plate than that for the thickest plate studied which is possibly due to the higher elastic flexural rigidity of a thick plate. Except for the 12.32 mm thick panel, the other four plates are not quite flat when they revert back to the position of zero centroidal deflection.

For the configurations of the five plates depicted in Fig. 7, the maximum temperature rise of about 29°C and 23°C occurs, respectively, in the 3 mm and the 12.32 mm thick plates.

The reason for different separation distances between the impactor and the plates in Fig. 7 is that the results were printed at discrete values of time, and the values of  $t_f$  and configurations of null central deflection are best estimates derived from the output.

The time histories of strain energies of elastic deformations, kinetic energies, the contact force, and the total energy dissipated due to plastic deformations and material softening are plotted in Fig. 8. The final time corresponds to the instant of complete separation between the impactor and the plate. The elastic and the kinetic energy time histories of the five plates are qualitatively similar to each other. The energy dissipated in the thickest plate is highest even though the maximum effective plastic strain induced in it is small because more material has been deformed plastically. The elastic (first peak in the kinetic energy) energy of the thinnest plate attains its maximum value at 1.5 ms (1 ms) whereas the corresponding time for the thickest plate is 0.7 ms (0.5 ms). Since the

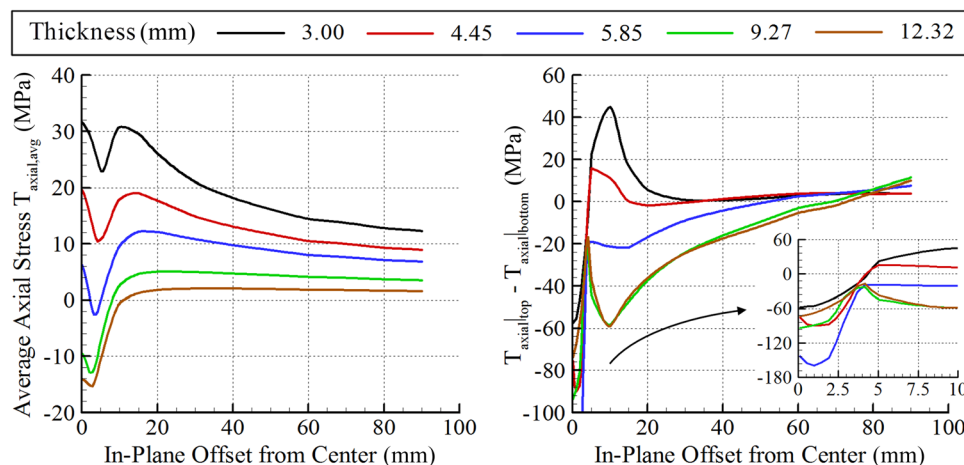


**Fig. 6 Average axial stress and difference between the average axial stress on the top and the bottom surfaces as a function of the  $x$ -coordinate along the centroidal axis for impact at 30 m/s of panels of different thicknesses**

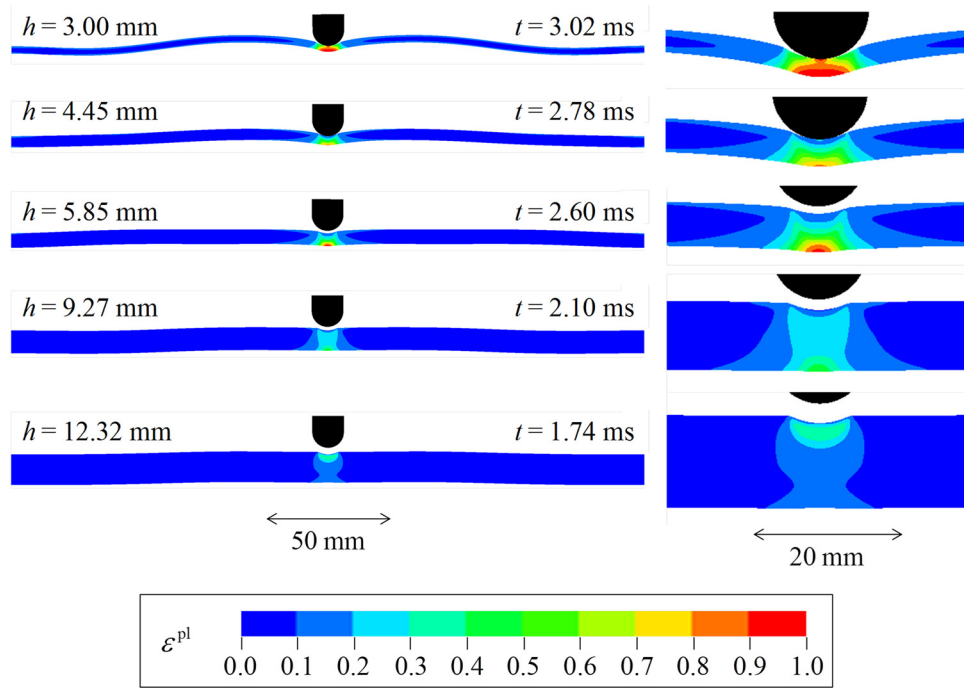


**Fig. 7** Fringe plots of the effective plastic strain in the deformed configurations corresponding to times when plates first revert back to the zero deflection position

plates are undergoing forced vibrations, these times need not be related to time periods of their free vibrations. We note that the maximum values of the elastic energy for the five plates are about the same but those of the maximum kinetic energy monotonically decrease with a decrease in the plate thickness. Note that the

minimum value of the kinetic energy does not equal zero since the velocity vectors differ from point to point. For each one of the five plates, the time of the maximum elastic energy nearly coincides with that of the first minimum in the kinetic energy of the panel, and the energy dissipated due to plastic deformations at

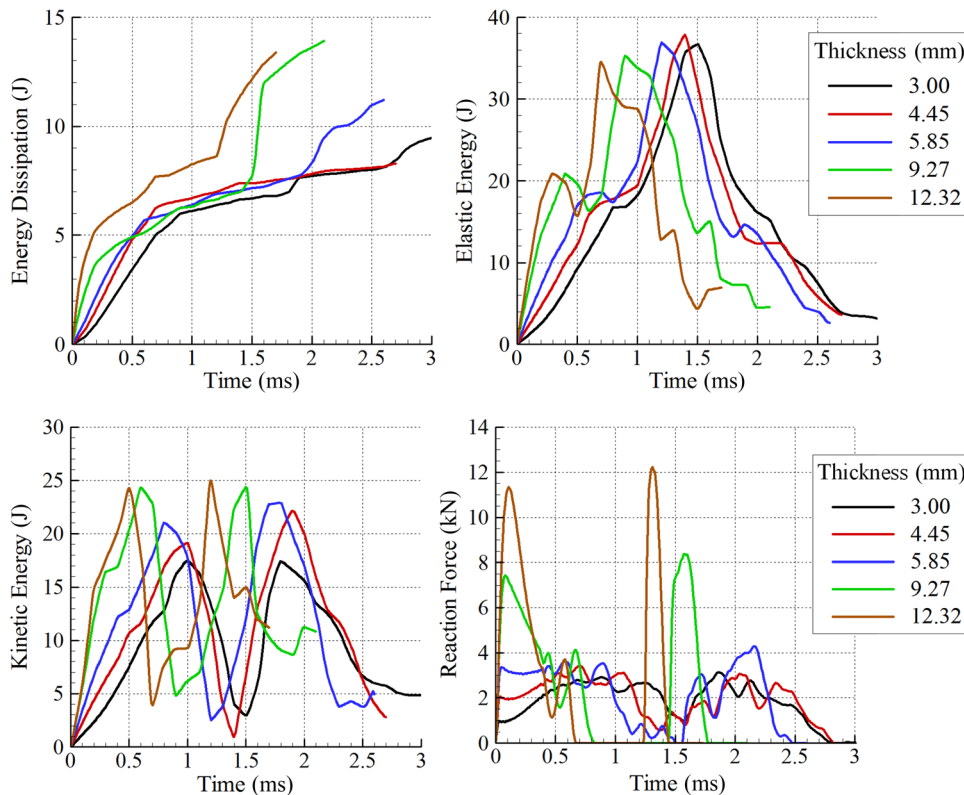


**Fig. 8** Time histories of the energy dissipated, the strain (elastic) energy, the kinetic energy, and the contact force of plates of different thicknesses impacted at 30 m/s

these times varies from about 12% of the initial kinetic energy of the impactor for the 3 mm thick plate to 24% for the 12.32 mm thick plate. Thus, it is not proportional to the plate thickness or volume. At time  $t_f$ , the energy dissipated equals 9.5 (20.3% of the initial kinetic energy of the impactor), 7.5 (16%), 11 (23.5%), 13.5 (28.9%), and 13 J (27.8%), respectively, for the 3, 4.45, 5.85, 9.27, and 12.32 mm thick plates and is not a monotonic function of the plate thickness. We recall that the initial kinetic energy of the impactor equals 46.8 J. Computations were not continued till the plate came to rest. Since only about 30% of the initial kinetic energy of the impactor has been dissipated due to inelastic deformations of a panel, computations will need to be continued for a long time for the panel to become stationary.

The maximum value of the reaction force between the impactor and the PC panel increases with an increase in the plate thickness. The contact force time histories for the 9.27 and the 12.32 mm thick plates differ qualitatively from those for plates of the other three thicknesses. For the thinner plates, once the contact between the impactor and the plate is lost, they stay separated but for the 9.27 and the 12.32 mm thick plates the contact stops after 0.8 and 0.65 ms, respectively, and is then re-established before the separation becomes final. The peak contact force for the 9.27 and the 12.32 mm thick plates is more than that for the thinner plates, and the value of the second peak contact force is higher than that of the first one. The times of the second peaks in the contact force seem to correspond to those of the second peaks in the kinetic energy time histories, however, there is no such correlation in the times of the first peaks in the contact force and the kinetic energy.

We define the axial stretch  $\lambda_{i_0}$  as the eigenvalue of the left Cauchy-Green tensor  $\mathbf{B}$  corresponding to the eigenvector of  $\mathbf{B}$  nearest to the deformed image of the vector  $\mathbf{N}$  which in the undeformed configuration is tangent to the midplane of the panel and points toward the center of the panel. That is,

$$i_0 = \operatorname{argmax}_i \left| \left( \frac{\mathbf{F} \cdot \mathbf{N}}{\|\mathbf{F} \cdot \mathbf{N}\|} \right) \cdot \mathbf{v}_i \right| \text{ with} \quad (5)$$

$$\mathbf{V} = \sqrt{\mathbf{B}} = \sqrt{\mathbf{F} \cdot \mathbf{F}^T} = \sum_{i=1}^3 (\lambda_i \mathbf{v}_i \otimes \mathbf{v}_i), \quad \|\mathbf{v}_i\| = 1$$

This definition is motivated by the expectation that at least one eigenvector of  $\mathbf{B}$  is tangent to the midplane of the deformed panel. For all problems studied here, it was found that the vectors  $\mathbf{v}_i$  and  $\mathbf{F} \cdot \mathbf{N}$  formed an angle whose cosine was larger than 0.9 in magnitude. Thus, the vectors  $\mathbf{v}_i$  and the vector into which  $\mathbf{N}$  is deformed were always nearly collinear. With  $\mathbf{n}$  denoting a unit vector into which  $\mathbf{N}$  is deformed, the axial stretch along  $\mathbf{n}$  is given by  $\sqrt{\mathbf{n} \cdot \mathbf{B} \mathbf{n}}$ . However, the unit vector  $\mathbf{n}$  may not be normal to the centroidal axis of the deformed plate. One could potentially plot the

square root of  $\mathbf{N} \cdot \mathbf{C} \mathbf{N}$  along the Z-axis in the undeformed configuration. Here,  $\mathbf{C}$  is the right Cauchy-Green tensor. Whereas tensors  $\mathbf{B}$  and  $\mathbf{C}$  have the same eigenvalues, their eigenvectors are directions of principal stretches in the deformed and the undeformed configurations, respectively. The value of  $\lambda_{i_0}$  approximately represents the axial stretch at a point in the deformed configuration.

The value of the axial stretch  $\lambda_{i_0}$  less (greater) than 1 implies that the length of the line element decreases (increases) after deformation, and  $\lambda_{i_0} = 1$  means that there is zero axial strain. For the 5.85 mm thick plate, we have depicted in Fig. 9 the axial stress  $\hat{T}_{\text{axial}}$  (see Eq. (4)) and the axial stretch  $\lambda_{i_0}$  versus the in-plane distance from the plate center (measured in the undeformed configuration) on the top ( $Z=0$ ), the mid ( $Z=-h/2$ ), and the bottom ( $Z=-h$ ) surfaces at the time when the impactor just separates from the panel. It is clear that a very small portion of the plate near the top surface is compressed and the rest of the region is stretched. The axial elongation is dominant near the bottom central part of the plate and even the midsurface is stretched. Thus, stretching deformations dominate over those due to bending. At points about 90 mm from the plate center, the bottom (top) surface is in compression (tension) signifying that the plate is bent concave down. The portion of the plate located at least 60 mm away from the Z-axis has undergone bending deformations. In the portion of the plate for which  $7 \text{ mm} < X < 40 \text{ mm}$ , the tensile axial stress on the top surface is generally less than the magnitude of the axial compressive stress on the bottom surface even though the axial elongation of the top surface is more than the axial contraction of the bottom surface. In the central portion, the top surface is in compression, and the bottom and the mid surfaces are in tension. Thus, deformations of the plate are quite complicated.

In Fig. 10, we have plotted through-the-thickness variation of the axial stress  $\hat{T}_{\text{axial}}$  and the axial stretch  $\lambda_{i_0}$  on the line passing through the plate centroid that also passes through the center of impact at times corresponding to those given in Fig. 7. Note that the initial Z-coordinates are normalized with respect to the undeformed plate thickness, thus zero corresponds to the top face of the plate and  $-1$  to the bottom one. For the 3, 4.45, and 5.85 mm thick plates, only a very small portion near the top surface is compressed, and most points including that on the midsurface are stretched. For the 9.27 and the 12.32 mm thick plates, all points on this line experience axial tension. Thus, according to the classical definition of the neutral surface (i.e., the surface on which the length of a line element remains unchanged) there is no such surface for the 9.27 and the 12.32 mm thick plates. The through-the-thickness variation of the axial stretch for the 3 and the 4.45 mm, thick plates are qualitatively different from those of the other three plates. One will need to investigate deformations of plates of different thicknesses between 4.45 mm and 5.85 mm to determine when the transition in the qualitative behavior occurs. The

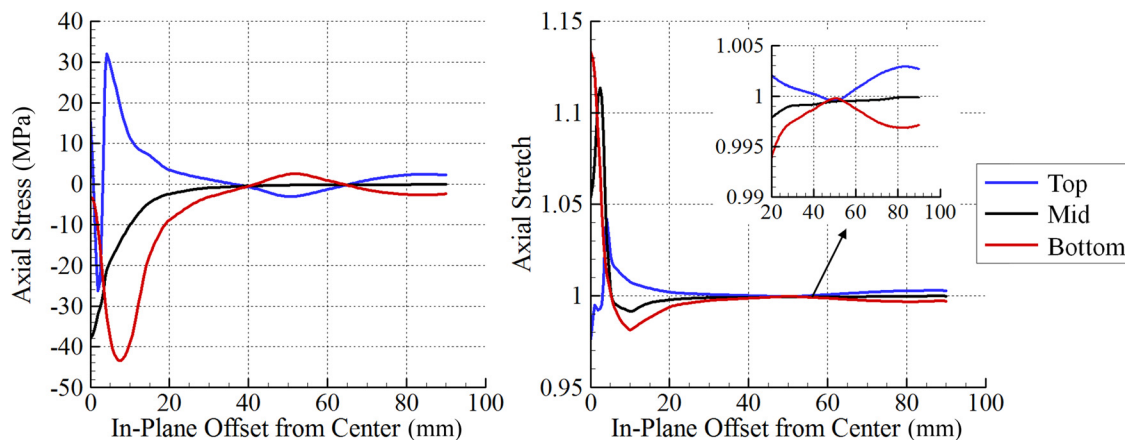
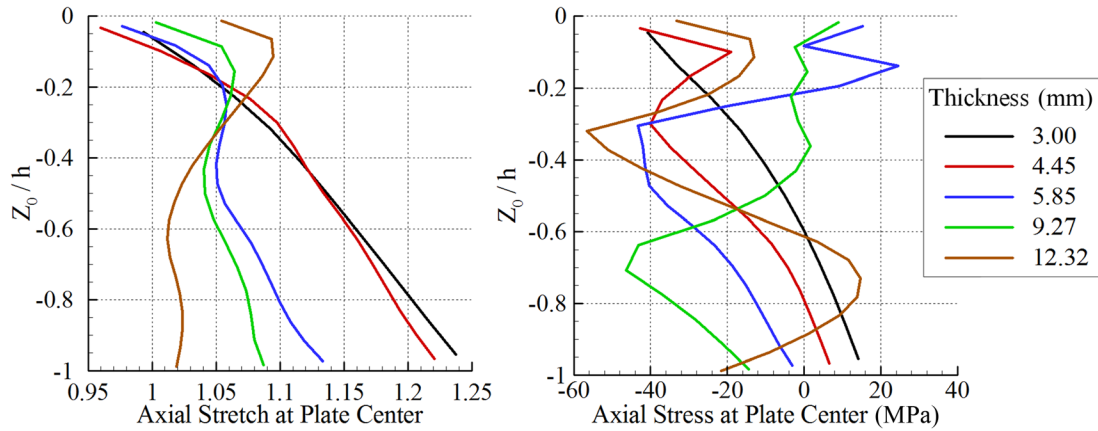


Fig. 9 Axial stress and axial stretch as a function of the distance from the plate center at the top, the mid- and the bottom surfaces of the 5.85 mm thick plate for 30 m/s impact velocity at the time  $t_f = 2.60$  ms



**Fig. 10** Through-the-thickness variation of the axial stretch and the axial stress on the centroidal axis for the 3, 4.45, 5.85, 9.27, and 12.32 mm thick plates and 30 m/s impact velocity at the times  $t_i$  of Fig. 7

resultant axial force can be computed by integrating  $\hat{T}_{axial}$  over the thickness. We thus see that the axial force for plates of all thicknesses considered is compressive implying that both bending moment and axial force act on an infinitesimal cross section since we have not integrated along either the  $X$ - or the  $Y$ -direction. For each plate points where the axial stress equals zero do not coincide with those where the axial stretch equals 1.

**4.1.3 Effect of Impact Velocity for the 5.85 mm Plate Thickness.** In this subsection, we study and compare results for impacts of the 5.85 mm thick plates by the smooth 104 g hemispherical-nosed impactor of radius 6.35 mm for impact speeds of 10, 20, 30, 40, and 50 m/s.

In Fig. 11, we have plotted the variations along the centroidal  $x$ -axis of the  $T_{axial}$  and the  $T_{axial,avg}$  as defined in Eq. (4). At the plate center, the sign of  $T_{axial,avg}$  is negative for impact speeds of 10 and 20 m/s but positive for the other three impact speeds. The spatial variations of  $T_{axial,avg}$  and of the difference in the values of  $T_{axial}$  on the top and the bottom surfaces are essentially similar for the five impact speeds considered.

For each impact speed we have exhibited in Fig. 12 the spatial distribution of the effective plastic strain on a plane section perpendicular to a plate edge and passing through the plate centroid. It is clear that plastic strains are localized in a narrow region near the plate center and as expected the size of the plastically deformed region as well as the maximum effective plastic strain increases with an increase in the impact speed. The maximum

effective plastic strain equals 0.23, 0.50, 0.94, 1.2, and 1.4, respectively, for 10, 20, 30, 40, and 50 m/s impact speed which shows that it is not proportional to the initial kinetic energy of the impactor because they do not form a geometric series. Except for the impact speed of 10 m/s, the largest values of the effective plastic strain occur at points near the bottom face of the plate and effective plastic strains on the top face of the plate are generally much smaller than those at corresponding points on the bottom face of the plate. How much of this difference is due to the magnitude of the yield stress of the PC being smaller in tension than that in compression remains to be investigated. For the impact speed of 50 m/s, the maximum temperature rise locally is about 32.5°C. For a room temperature of 25°C, the maximum temperature of 57.5°C is way below the melting temperature of about 155°C. However, Young's modulus of the material point could significantly decrease from its value at the room temperature. We recall that the temperature dependence of Young's modulus depicted in Fig. 27 has been considered. For this local temperature, we did not observe localization of deformation into shear bands as reported in Ref. [19] for high strain-rate plane strain deformations of PC specimens.

The time histories of the kinetic, the elastic, and the dissipated energies of the plates normalized by the initial kinetic energy of the impactor and of the reaction force between the impactor and the plate are depicted in Fig. 13. With an increase in the impact speed, a larger portion of the initial kinetic energy of the impactor is used to plastically deform the plate, and the time of separation

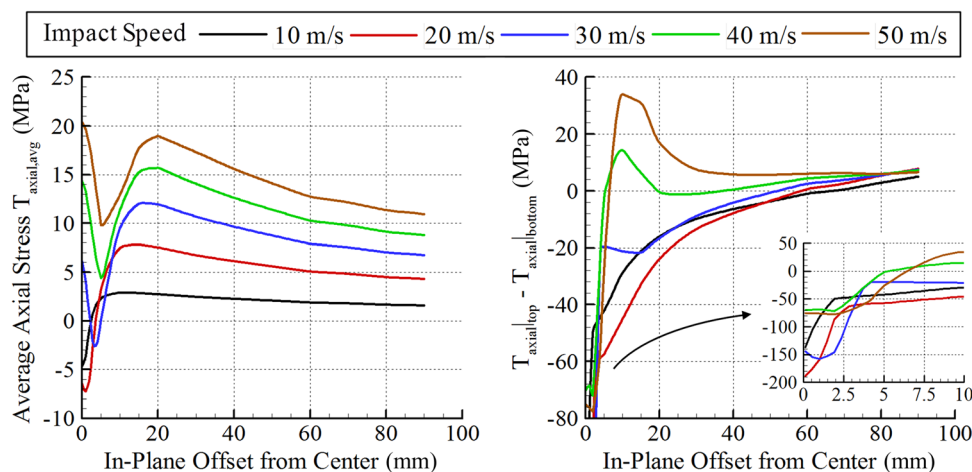


**Fig. 11** Average axial stress and difference between the average axial stress on the top and the bottom surfaces as a function of the  $X$ -coordinate along the centroidal axis for impact of the 5.85 mm thick panel at different speeds

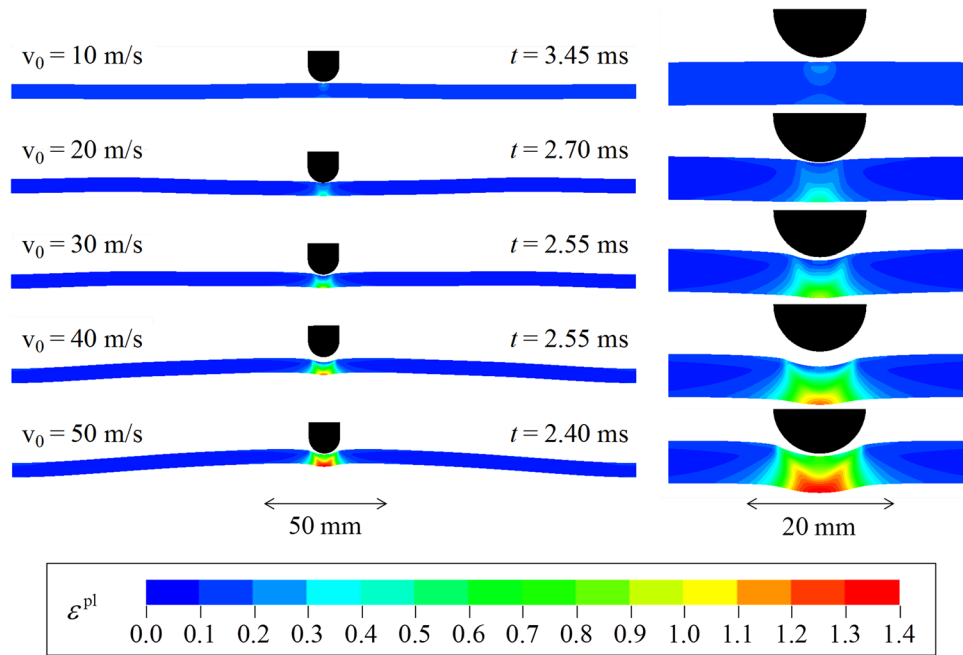


**Fig. 12** Fringe plots of the effective plastic strain in the deformed configurations at the times of separation between the 5.85 mm thick plate and the impactor. The times of separation are also listed.

of the impactor from the plate monotonically decreases with an increase in the impact speed. The times of the initial peaks in the elastic and the kinetic energies also monotonically decrease with an increase in the kinetic energy of the impactor. However, the qualitative nature of these plots remains unaffected by the impact speed. The maximum value of the reaction force is nearly

proportional to the impact speed which agrees with the results of Her and Liang [26].

Similar to the results plotted in Figs. 9 and 10, we have exhibited in Figs. 14 and 15 the axial stress and the axial stretch as a function of the distance from the plate center for the impact speed of 50 m/s and through-the-thickness distribution of the axial stress

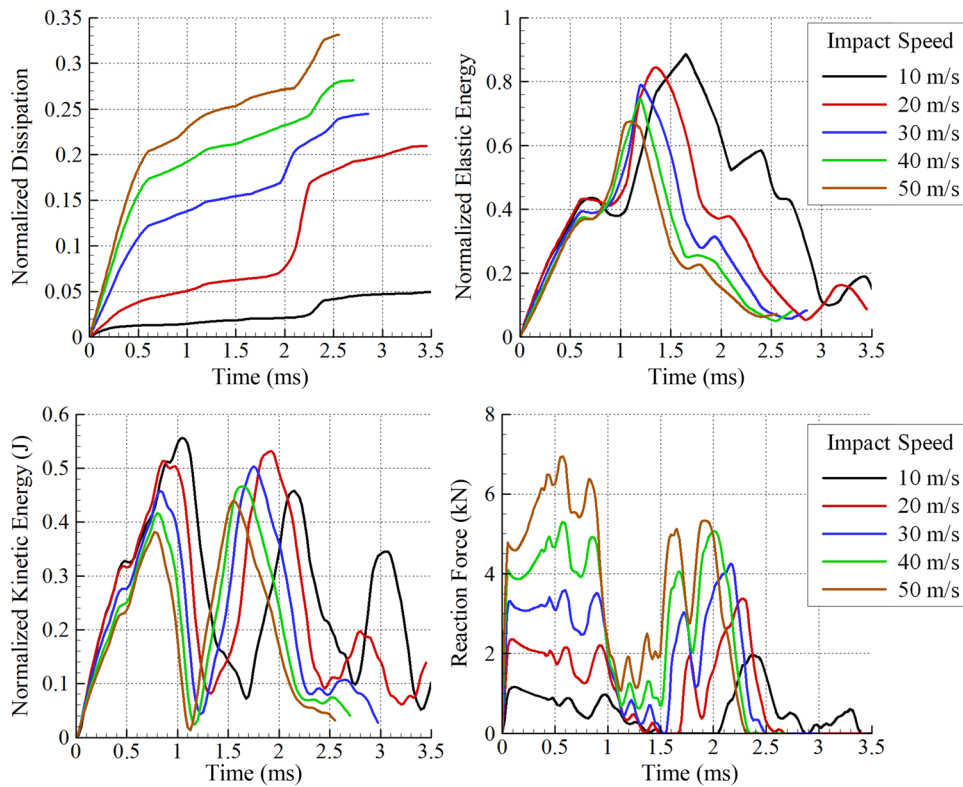


**Fig. 13** Time histories of the normalized energy dissipated, the normalized strain (elastic) energy, the normalized kinetic energy, and the contact force for the 5.85 mm thick plate for different impact speeds. Energies are normalized by the initial kinetic energy of the impactor.

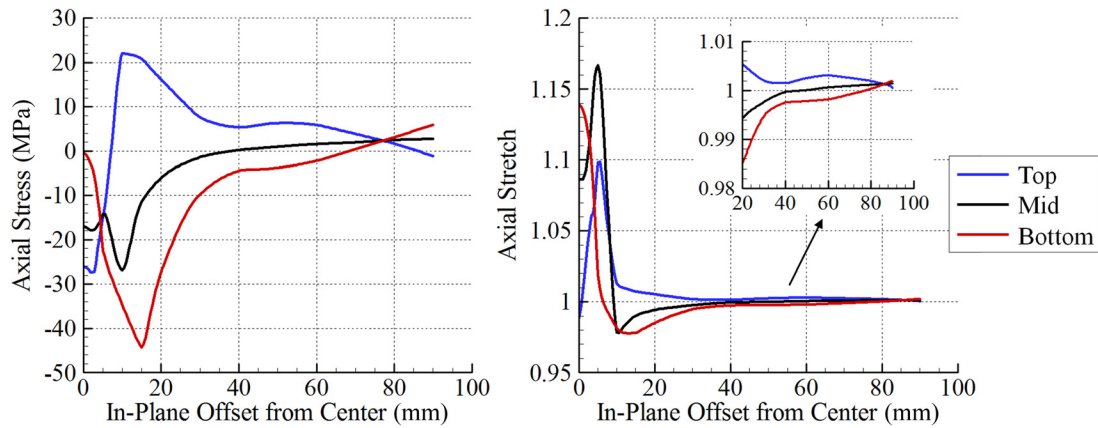


**Fig. 14** Axial stress and axial stretch as a function of the distance from the plate center at the top, midplane, and bottom of the PC plate for 50 m/s impact velocity and at the final time  $t_f = 2.40$  ms

and the axial stretch for different impact speeds. We see that far from the plate center the magnitude of the axial stress on the mid surface is much smaller than that on the top and the bottom surfaces which have opposite signs, indicating there the dominance of bending deformations. Close to the plate center, points on the top, the mid, and the bottom surface are axially stretched. However, at 10 mm from the plate center points on the top surface are axially stretched and those on the mid and the bottom surfaces are axially compressed.

Through-the-thickness variations of the axial stretch for impact speeds of 20, 30, 40, and 50 m/s are quite different from that for the impact speed of 10 m/s. Except for the impact speed of 10 m/s, axial lines at all points except those close to the top surface have been elongated as indicated by values of the axial stretch greater than 1. For the impact speed of 10 m/s, the length of several axial line elements has remained unchanged. The axial elongation at the plate bottom surface monotonically increases with an increase in the impact speed. For each impact speed, the resultant axial force on an infinitesimal area is negative, and points where the axial stress vanishes do not coincide with those where the axial stretch equals 1.

**4.2 Curved Panels.** In order to study the effect of the curvature on the impact response of clamped panels, we consider  $254 \times 254$  mm panels of different thicknesses having the two equal principal radii,  $R = -127, -254, -508, \pm\infty$  (flat plate), 508, 254, and 127 mm.

**4.2.1 Quasi-Static Indentation.** For a cylindrical impactor of nose radius 6.35 mm (see Fig. 1), we have plotted in Fig. 16 the

computed contact force as a function of the quasi-static indentation depth. Quasi-static deformations were simulated by increasing the mass density of the panel material so that the time for an elastic wave to propagate to the panel edge was nearly 1/1000 of the final time of the computed deformation. The kinetic energy of the panel equaled less than 1% of its total strain energy of deformations for material properties at the strain rate of 0.001/s thereby ensuring that deformations analyzed were quasi-static.

We have listed in Table 2 the values of the initial stiffness, i.e., slope of the contact force versus the indentation depth curves for the five values of the plate thickness. These results evince that the initial resistance to indentation of a panel increases with an increase in the panel curvature (or decrease in the radius of curvature) for plates with both positive (concave down) and negative (concave up) curvatures. These results qualitatively agree with those of Kim et al. [23] and Lin and Lee [27]. However, the variation of the contact force with the indentation for thin panels is qualitatively and quantitatively different for panels of positive and negative curvature. For panels of negative curvature, the contact force is nearly proportional to the indentation, while the tangent stiffness for the positively curved panels decreases with an increase in the indentation. For the 3 mm thick panels and the 12.5 mm indentation, the contact force for the panel with  $R > 0$  is nearly four to eight times that of the panel of negative curvature but having the same magnitude of  $R$ . For thicker panels, however, the effect of the sign of the curvature is small and the magnitude of the curvature determines the response of the plate. For example, the initial tangent stiffness of the 5.85 (length of side/thickness = 43.4), 9.27, and the 12.32 mm thick panels listed in Table 2 is nearly the same for positive and negative values of  $R$ .

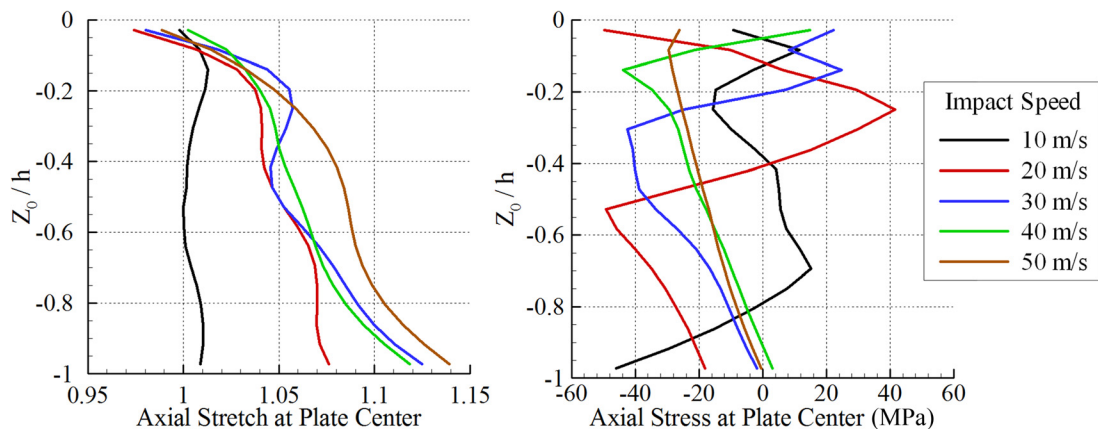


**Fig. 15** Axial stretch and axial stress at the plate center as a function of the initial  $Z$  position for 10, 20, 30, 40, and 50 m/s impact speeds at the times  $t_f$  of Fig. 12

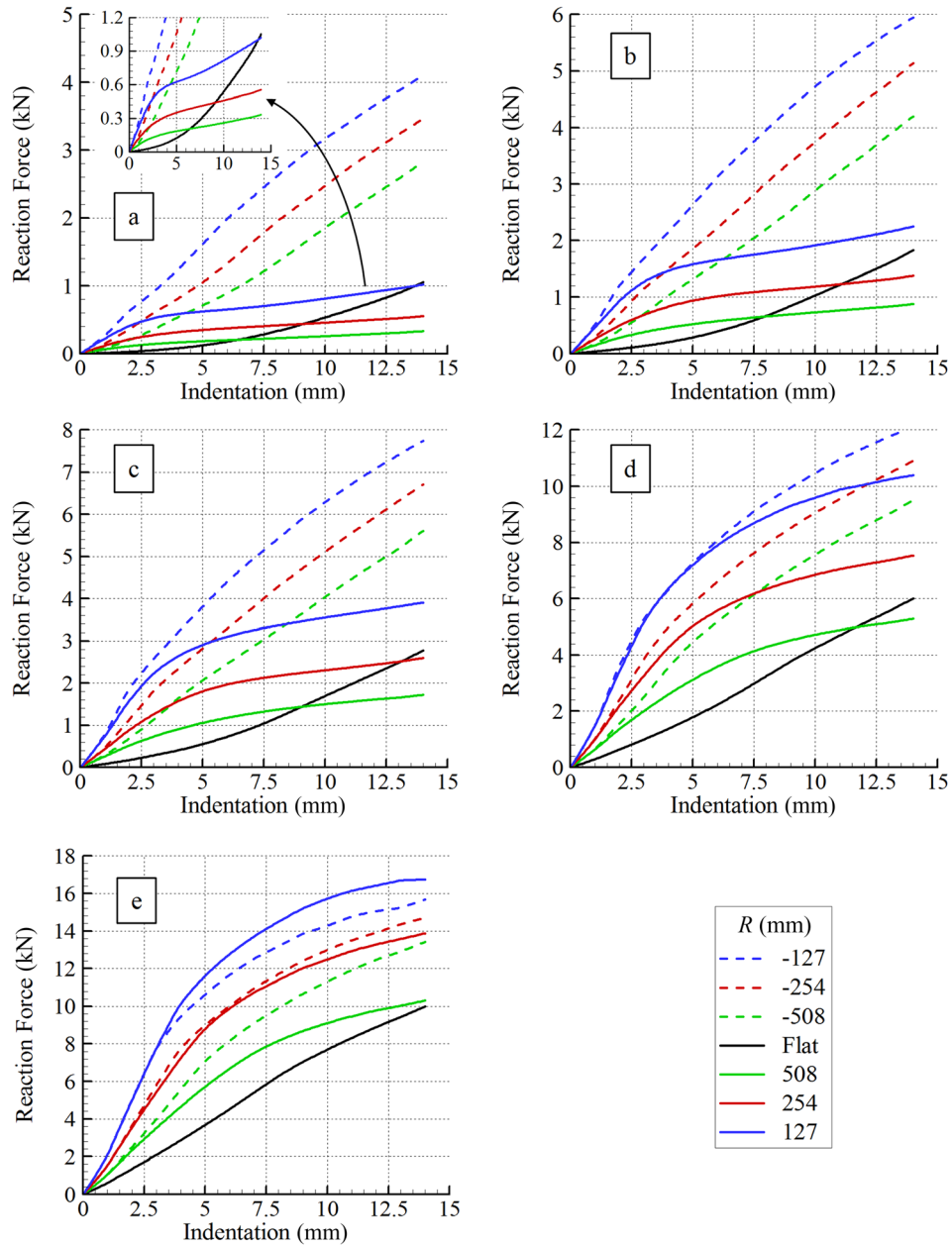


**Fig. 16** Contact force versus indentation for the (a) 3.00, (b) 4.45, (c) 5.85, (d) 9.27, and (e) 12.32 mm thick panels of different radii of curvature

Thus, the effect of the sign of curvature on the initial stiffness becomes negligible for aspect ratios less than 43.

In order to investigate the effect of curvature on the stretching/bending of the panel, we use the variable  $T_{axial}$  defined by Eq. (4) with the difference that the time averaging is replaced by

**Table 2** Initial stiffness of curved panels in kN/mm

Plate thickness (mm)	Radius of curvature $R$ (mm)						
	-127	-254	-508	$\pm\infty$	508	254	127
3.00	0.27	0.15	0.081	0.011	0.064	0.12	0.22
4.45	0.51	0.29	0.17	0.038	0.15	0.26	0.46
5.85	0.79	0.47	0.29	0.084	0.26	0.44	0.75
9.27	1.5	1.0	0.67	0.29	0.64	1.0	1.5
12.32	2.1	1.5	1.1	0.60	1.0	1.5	2.1

averaging over the indentation depth. For a curved panel, the vector  $\mathbf{N}$  is orthogonal to the local cross section and points toward the panel center. The mean value of  $T_{axial}$  through the thickness measures the local stretching of the panel while the difference between its values at the top and the bottom of the panel for the same initial arc length is related to the local bending of the panel. Variations with the initial arc length,  $r$ , of  $T_{axial}$  and the difference in its values at corresponding points on the top and the bottom surfaces are shown in Figs. 17(a)–17(e) for the 3, 4.45, 5.85, 9.27, and 12.32 mm thick panels. It is clear that both the panel thickness and the panel curvature influence bending and stretching deformations at a point. For  $R < 0$ , values of  $T_{axial,avg}$  at  $r=0$  decrease with an increase in the panel thickness. Bending deformations dominate only in a very small region near the center of a panel. In general, values of  $T_{axial,avg}$  do not vary monotonically with a change in the plate curvature. Because of the possibility of noticeable plastic deformations induced the present results cannot be directly compared with those for elastically deformed panels.

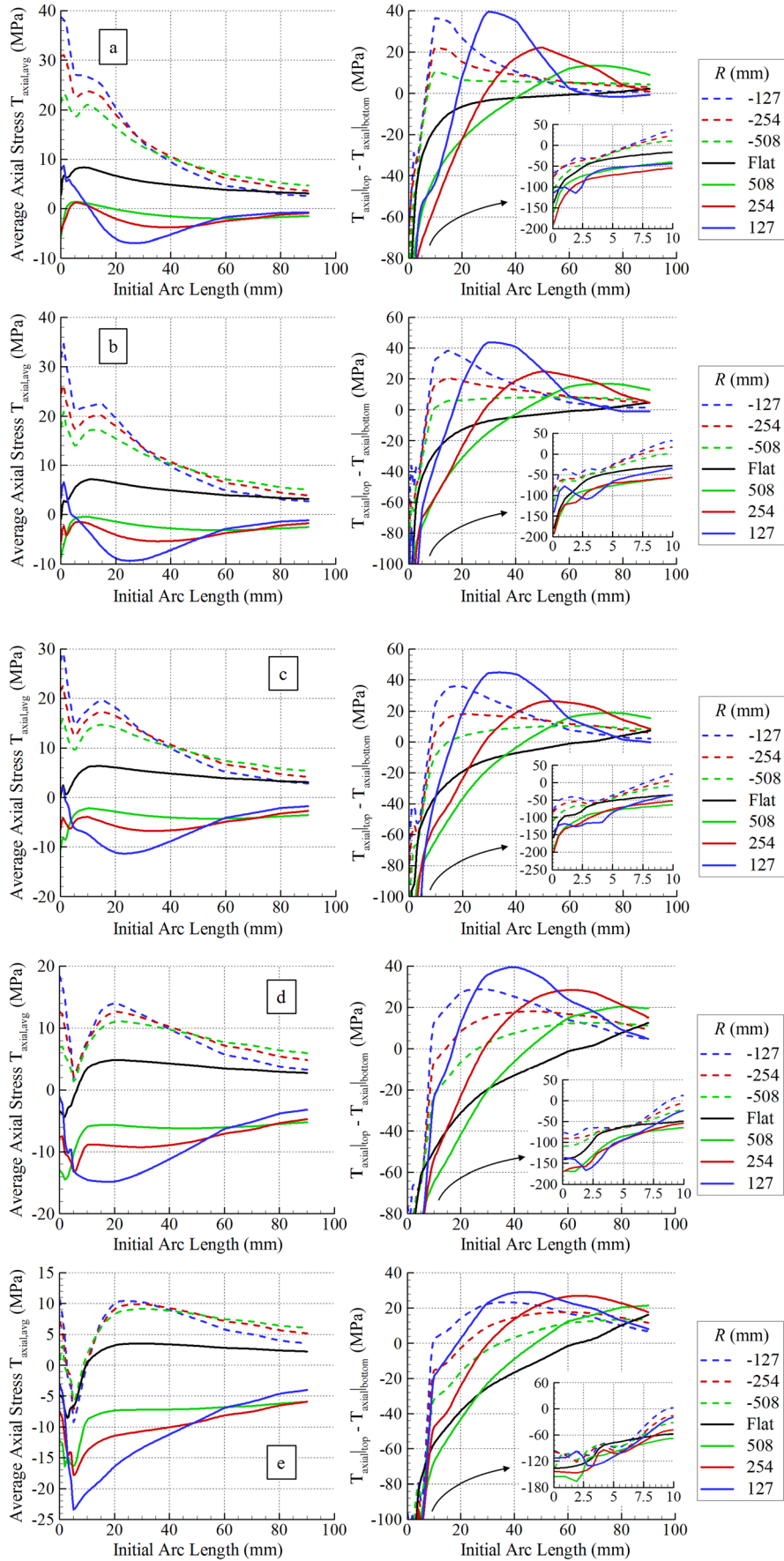


**Fig. 17** Average axial stress and the difference between the axial stress on the top and on the bottom surfaces of the (a) 3.00, (b) 4.45, (c) 5.85, (d) 9.27, and (e) 12.32 mm thick panels as a function of the initial arc length (measured from the panel center)

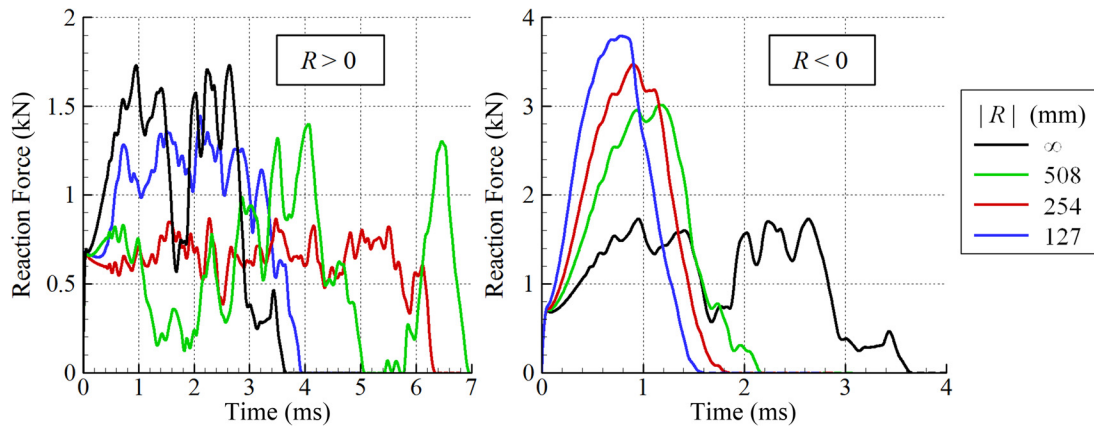


Fig. 18 Time histories of the contact force for 3 mm thick panels of different curvatures impacted at 20 m/s

### 4.3 Impact at 20 m/s

4.3.1 *Panels 3 mm Thick.* For different values of  $R$ , time histories of the reaction force between the 3 mm thick panel and the 104 g hemispherical-nosed cylindrical impactor traveling at 20 m/s are presented in Fig. 18. These results have been plotted till the time when the impactor finally separates from the panel. Whereas the time histories are quite smooth for panels with  $R < 0$ , they have high frequency components for panels with  $R > 0$ . For  $R < 0$ , the contact duration for  $R = 254$  mm is between that for  $R = 127$  and 508 mm. For  $R = 254$  mm, variations in the contact force during the time of contact are much smaller than those for other values of  $R$ . It seems that the contact duration is related to the panel static indentation stiffness (Fig. 16) as the panel with the highest value of the initial slope of the reaction force versus the indentation curve has the shortest impact duration. Below we

provide additional information on how the panel curvature affects its deformations.

Fringe plots of the effective plastic strain distribution on a cross section passing through the panel centroid when the impactor finally loses contact with it are depicted in Fig. 19. These results suggest that the impact responses of panels with the positive and the negative curvatures are noticeably different. Curiously enough the effective plastic strain distribution in the flat plate is qualitatively similar to that in the panel with  $R = 127$  mm rather than that in the panel with  $R = 508$  mm. The panel with  $R = 254$  mm has the least plastically deformed region, and the maximum effective plastic strain in it is smaller than that in the other six panels. The panel with  $R = -127$  mm has the largest plastically deformed region with the maximum effective plastic strain of about 1.4.

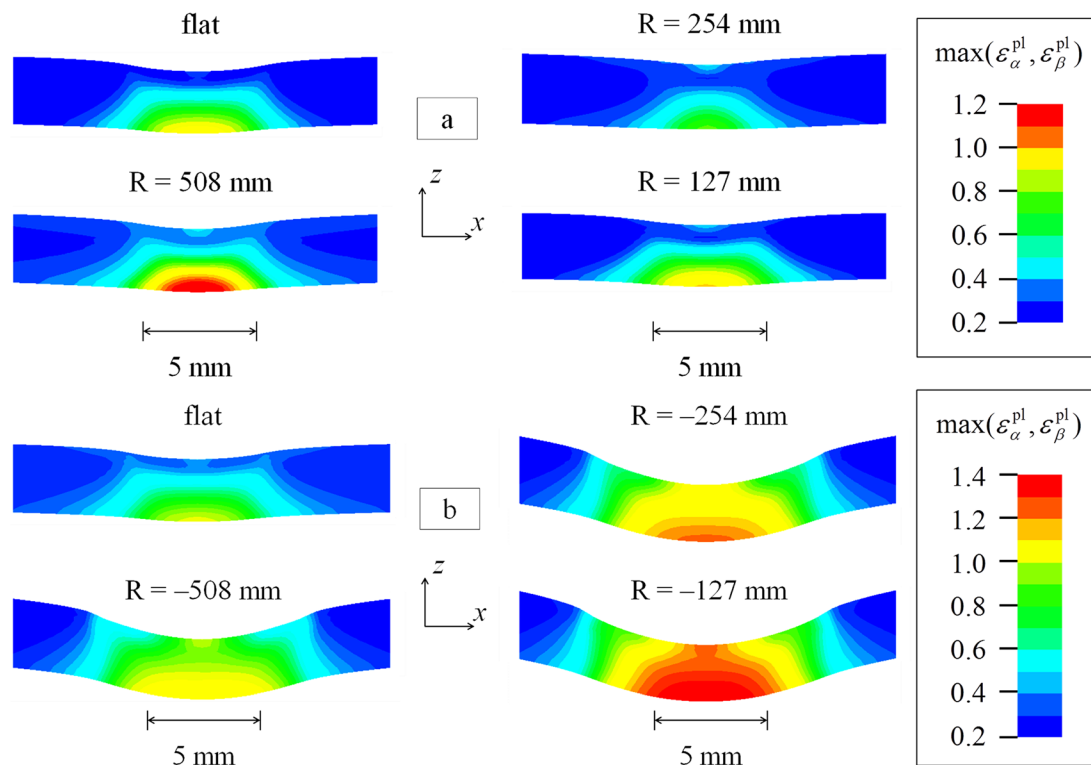
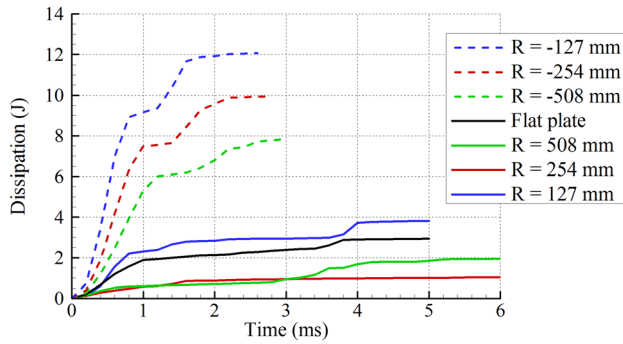


Fig. 19 Fringe plots of the effective plastic strain in the central region of a cross section passing through the centroid of the 3 mm thick panels with (a)  $R > 0$  and (b)  $R < 0$ . Note that values of fringes in Figs. (a) and (b) are different.



**Fig. 20 Time histories of the energy dissipation for 3 mm thick panels of different curvatures for impacts at 20 m/s**

Time histories of the total energy dissipated due to plastic deformations and material softening during the impact of the 3 mm thick panels are exhibited in Fig. 20. For panels with  $R < 0$ , the energy dissipation decreases with the increase in the magnitude of  $R$ , the energy dissipated is consistent with the plastic strain distribution in the neighborhood of the impact area shown in Fig. 19, and the energy dissipated is significantly more than that for panels with  $R > 0$ . Results for the flat plate are close to those of panels with  $R > 0$  and are generally closer to those of the panel with  $R = 127$  mm. The results are less intuitive for the panels with  $R > 0$  because the energy dissipated in the panel with  $R = 127$  mm is more than that in the panel with  $R = 508$  mm since the largest plastic strains occur in the later panel. However, these results can be explained by examining the distribution of the energy dissipation density on the bottom surface and through the thickness of the panels with  $R = 508$  and  $127$  mm, and evinced in Fig. 21. It is clear that the magnitude of the energy dissipation density is larger at the center of the back face of the panel with  $R = 508$  mm, but the dissipation density on the top surface of the panel as well as at points a few millimeter away from the panel center is less than that for the panel with  $R = 127$  mm. It explains the larger total energy dissipated despite the smaller value of the maximum effective plastic strain induced in the panel of  $R = 127$  mm. In order to further corroborate this observation, we introduce the function

$$f(r) = \int_{t=0}^{t_f} \left[ \int_{\Omega(r)} \left( \dot{W}_\alpha^{e,\text{soft}} + \dot{W}_\beta^{e,\text{soft}} + J\sigma_\alpha : \tilde{\mathbf{D}}_\alpha^p + J\sigma_\beta : \tilde{\mathbf{D}}_\beta^p \right) dV_0 \right] dt \quad (6)$$

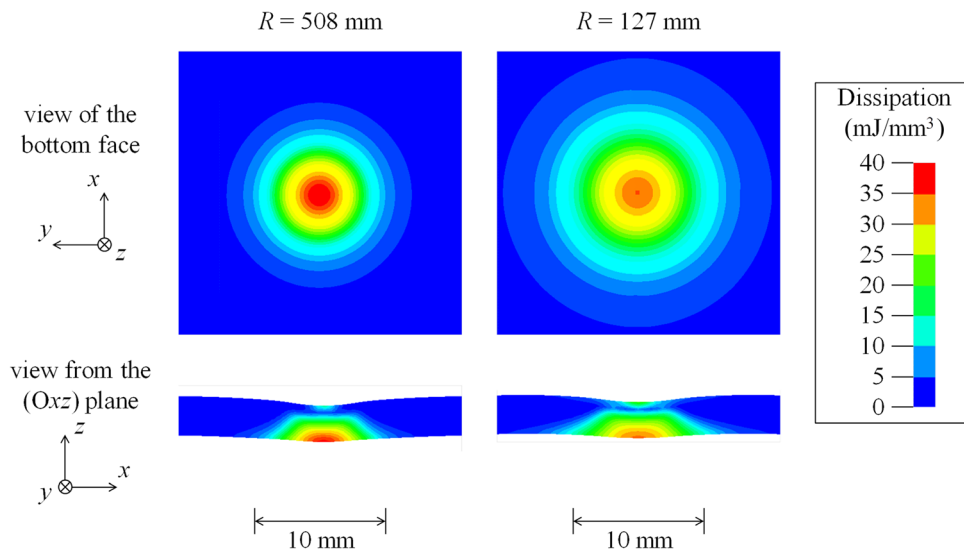


**Fig. 21 Fringe plots of the energy dissipation density on the back surface and through the thickness of panels with  $R = 508$  and  $127$  mm**

where  $\Omega(r)$  is the portion of the panel that is located inside the cylinder  $X^2 + Y^2 = r^2$  in the undeformed configuration. The function  $f$  measures the amount of energy dissipated in the portion of the panel initially (at time  $t=0$ ) located within a distance  $r$  from the axis  $X=Y=0$  of impact. In Eq. (A6), terms appearing on the right-hand side represent the energy dissipated due to softening and plastic deformations, and  $t_f$  is the time when the impactor finally separates from the panel. Since the volume over which  $f$  is computed varies with  $r$ , values of the function  $f$  will vary even if the integrand is a constant. Thus, one expects  $f$  to be essentially zero at  $r=0$ . Values of  $f$  versus the radius  $r$  are plotted in Fig. 22 for two curved panels with  $R = 127$  and  $508$  mm. These plots reveal that the energy dissipated near the center of impact is about the same for the two panels, and the larger energy dissipation in the panel with  $R = 127$  mm is mainly due to the higher value of the energy dissipated in the region located at distance between 3 and 10 mm from the center of impact. This explains the counter-intuitive result that larger plastic strains near the center of the panel do not necessarily imply larger energy dissipation. Whereas there is energy dissipated in the region with  $r > 50$  mm for the flat plate and in the curved panel of  $R = 508$  mm, there is essentially no energy dissipated in this region for the panel with  $R = 127$  mm.

**4.3.2 Panels of Different Thicknesses.** Variations with  $r$  of  $T_{\text{axial}}$  are shown in Figs. 23(a)–23(e) for the 3, 4.45, 5.85, 9.27, and 12.32 mm thick panels. We recall that  $T_{\text{axial}}$  measures the local stretching of the panel while the difference between its values at the top and the bottom surfaces of the panel for the same initial arc length is related to the local bending.

It is evident from the results plotted in Fig. 23 that the curvature of the panel strongly influences the average stress  $T_{\text{axial,avg}}$ . The negative (positive) curvature increases (decreases) the tensile axial stress near the center of the contact area. For panels with negative (positive) curvature, the average axial stress near the panel edges is compressive (tensile). Results for the flat plate are qualitatively similar to those for a panel of positive curvature. For the 3 and the 4.45 mm thick panels, the stress distributions for  $R = 127$  mm are quite different from those in panels with  $R = 254$  and  $508$  mm in the sense that the average tensile axial stress near the center is much larger and drops rapidly to become larger in compression for arc length in the reference configuration of more than 10 mm. Results plotted in Fig. 23 (right) suggest that bending effects are more dominant in panels with positive curvatures. We notice in particular that for the thickest panels (9.27 and 12.32 mm), the sign of the curvature has negligible influence on the

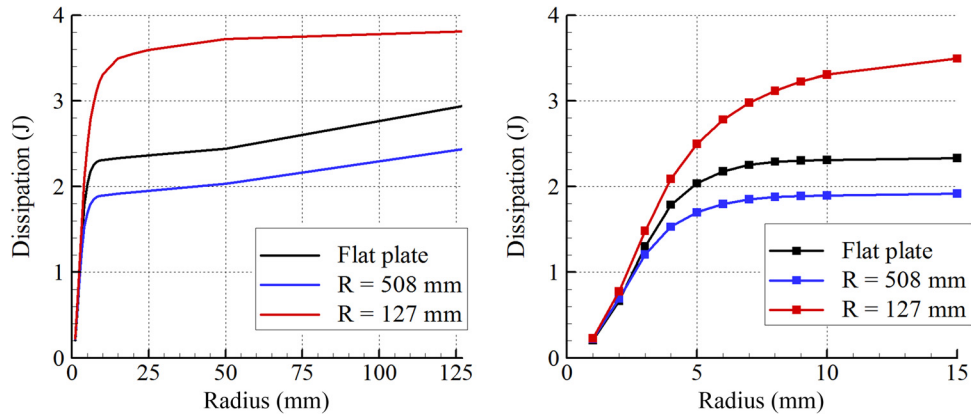


**Fig. 22** Variation of the energy dissipation represented by the function  $f(r)$  with the radius for the flat and the curved panels of  $R = 127$  and  $508$  mm. The figure in the right is a blow-up of that on the left for small values of  $r$ .

bending of the plate while it has a major impact on the average axial stress  $T_{axial,avg}$ . This is further elucidated upon below by additional results provided for the 12.32 mm thick panels.

For the 12.32 mm thick panels of various curvatures and 20 m/s impact speed, the postimpact contours of the effective plastic strain are depicted in Fig. 24 at times when the impactor definitely separates from the panels. The largest values of the effective plastic strain occur in the flat panel. Overall the effective plastic strains developed in the 12.32 mm thick panels are much smaller than those in the 3 mm thick panels. While negative curvatures considerably degraded performances of the 3 mm thick panels it is not the case for the 12.32 mm thick panels. Fringe plots of Fig. 24 indicate that the largest effective plastic strains do not occur at points on the rear face of the panels (which is the case for the 3 mm thick panel for which fringe plots are depicted in Fig. 19) and that the regions of noticeable effective plastic strains are narrow (about the same radius as that of the impactor) and about 5 mm deep.

We have exhibited in Figs. 25(a) and 25(b) the axial stress and the axial stretch as a function of the distance from the plate center for the 3 and the 12.32 mm thick panels with the radius of curvature,  $R = \infty$ , 127 mm, and  $-127$  mm. In Fig. 26, we have plotted through-the-thickness variations of the axial stress and the axial stretch on the centroidal axis. In these figures, the curves for panels with  $R = \infty$  (i.e., flat), 127 mm, and  $-127$  mm correspond to  $t = 3.6$  (1.5), 3.8 (0.68), and 1.6 (0.65) ms for the 3.00 (12.32) mm thick plate, respectively. For the 3 mm thick flat plate, the axial stress is tensile on a significant portion of the central region at points on the top surface and compressive at points on the mid- and the bottom surfaces. The signs of the axial stress reverse from tensile to compressive at points situated more than 40 mm from the centroidal axis. Except for the magnitudes, the qualitative distributions of the axial stress are the same. The plate with  $R = 127$  mm has the maximum magnitude of the compressive axial stress, while the plate with  $R = \infty$  has a higher value of the maximum tensile stress than the plates with  $R = 127$  and  $-127$  mm. For the plate with  $R = -127$  mm, the central portion of the midsurface that has large values of the axial stretch extends further out than that for plates with the other two values of  $R$ . A small central region of the top surface for the two plates with  $R = \infty$  and 127 mm is compressed. However, for the plate with  $R = -127$  mm, the entire top surface has positive values of the axial stretch with the maximum value occurring at a point situated about 8 mm from the centroidal axis. Thus, the plate curvature influences whether the central portion of the plate surrounding the centroidal axis is compressed or stretched and the maximum magnitude of the axial stretch induced there.

Referring to Fig. 25, we see that for the 12.32 mm thick flat plate, the axial stress at points on the bottom, the mid-, and the top surface that are quite close to the centroidal axis is tensile. However, as one

moves away from the centroidal axis, it becomes compressive at points on the top surface, zero at points on the midsurface but stays tensile at points on the bottom surface. For the curved plate with  $R = -127$  mm, the axial stress is compressive at all points on the mid and the bottom surfaces but on the top surface it switches from tensile at points close to the centroidal axis to compressive at points located about 6 mm away from the centroidal axis. When  $R = 127$  mm, the axial stress at all points on the top and the midsurfaces is tensile and that on the bottom surface is compressive at points near the centroidal axis but tensile at points at least 20 mm away from this axis. The maximum magnitude of the axial stress is for the plate with  $R = 127$  mm and occurs at a point 2 mm away from the centroidal axis. Thus, the distribution of the axial stress on the three surfaces strongly depends upon the plate curvature. The axial strains ( $=$ (axial stretch  $- 1$ )) are small at all points with the maximum axial strain equaling about 6.5%, and it occurs at points located about 3 mm from the centroidal axis. The maximum axial strain is higher in the plate with  $R = -127$  mm than that in the flat plate. Thus, the plate that has the maximum axial tensile stress developed in it does not have the maximum axial tensile strain.

The through-the-thickness variations of the axial stretch plotted in Fig. 26 for the 3 mm thick plate are quite different, both qualitatively and quantitatively from those for the 12.32 mm thick plate. In the 12.32 mm thick plate with  $R = -127$ ,  $\infty$ , and 127 mm, there is practically no axial strain in the bottom 1/4th of the plate near the centroidal axis, with the remaining portion having tensile axial strain. The maximum value of the axial strain occurs at points nearly 1/10th plate thickness below the top surface. In the thin plate with  $R = -127$ ,  $\infty$ , and 127 mm, the axial strain is tensile through most of the plate thickness and is compressive at points near the top surface for plates with  $R = \infty$  and 127 mm. The through-the-thickness axial stress distribution is smoother in the 12.32 mm thick plate for the three values of  $R$  and in the 3 mm thick curved plate with  $R = 127$  mm than that in the 3 mm thick plate with  $R = \infty$  and  $-127$  mm. The integral of the axial stress over the plate thickness has a negative value, except for the 3 mm thick plate with  $R = -127$  mm. Thus, there is a resultant axial force and a bending moment acting on both thin and thick plates for all three values of  $R$ .

We note that the yield stress of the PC in uniaxial tension is about 23% less than that in uniaxial compression. Quantifying its effect on plate's deformations is rather arduous and has not been attempted here.

## 5 Conclusions

We have analyzed by the FEM transient large deformations of clamped flat and curved (both concave upward and downward) PC panels of five different thicknesses impacted at

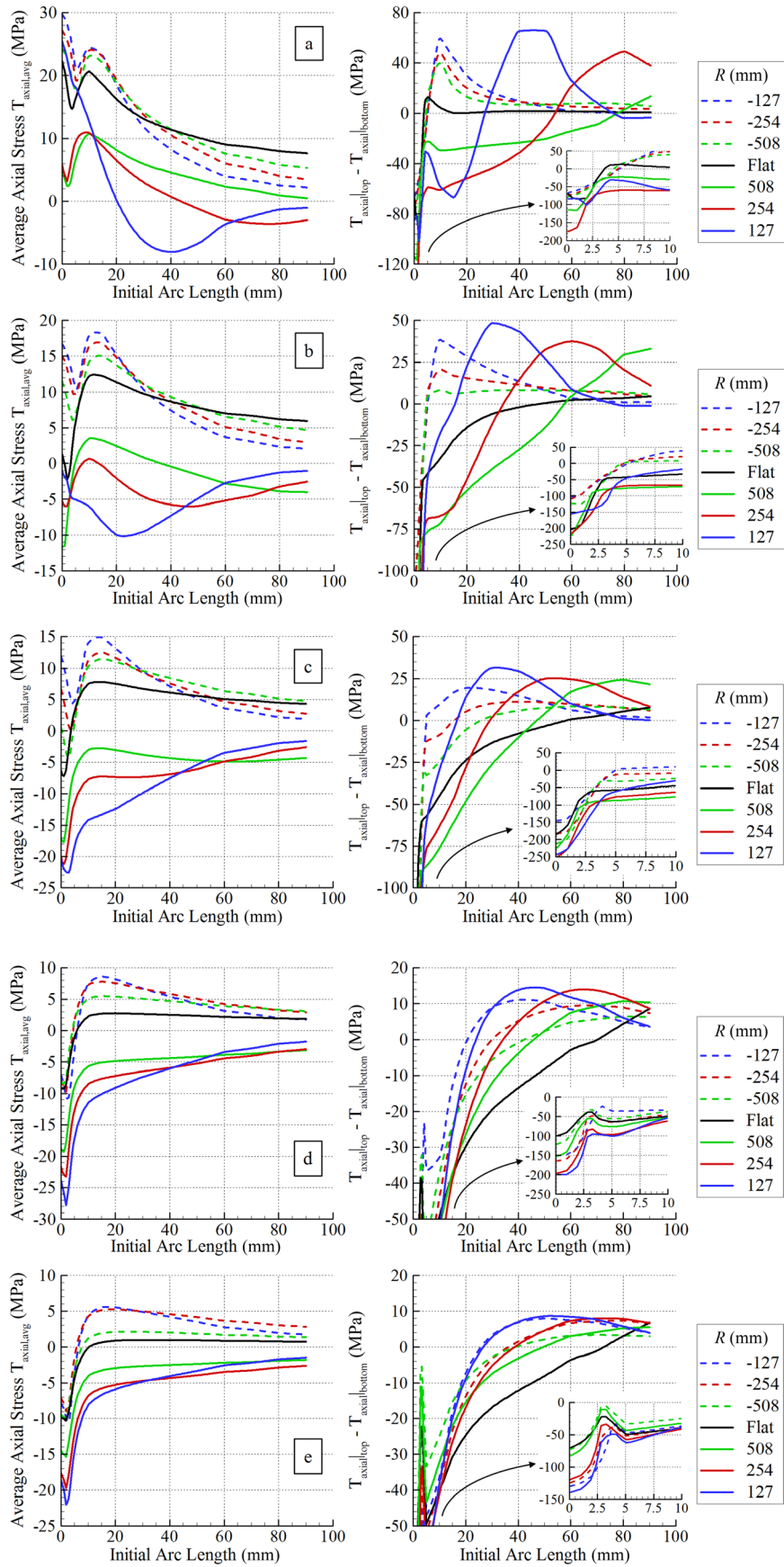


**Fig. 23** Average axial stress and the difference between the axial stress on the top and on the bottom surfaces of the (a) 3 mm, (b) 4.45 mm, (c) 5.85 mm, (d) 9.27 mm, and (e) 12.32 mm thick panels as a function of the initial arc length (measured from the panel center)

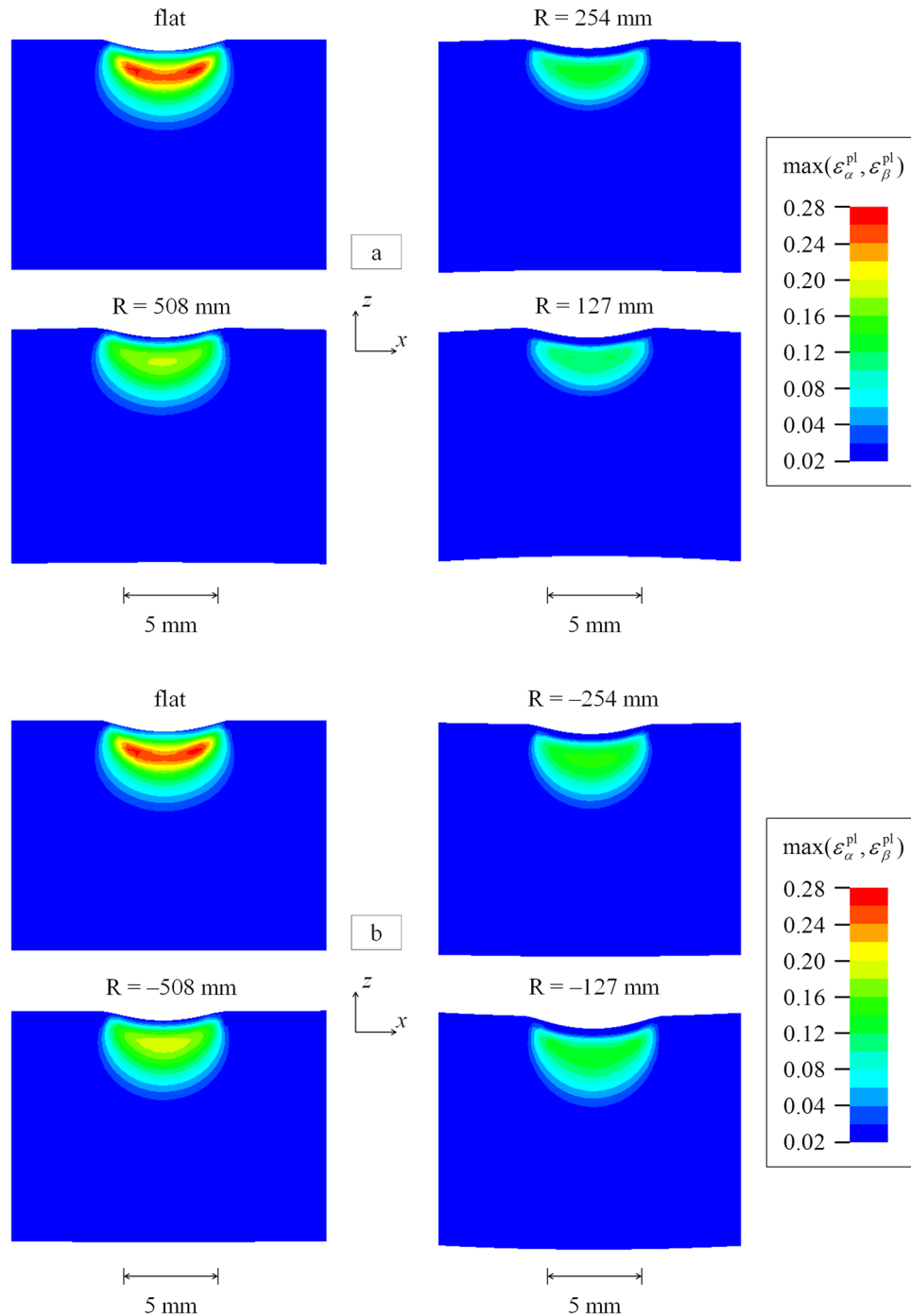


**Fig. 24** Fringe plots of the effective plastic strain in the central region of a cross section passing through the centroid of the 12.32 mm thick panels with (a)  $R > 0$  and (b)  $R < 0$

normal incidence at the center by a 104 g hemispherical-nosed steel cylinder moving with a maximum speed of 50 m/s. The PC has been modeled as thermo-elasto-viscoplastic, the steel cylinder as rigid and the contact between the panel and the cylinder as smooth. The peak computed deflections of the clamped square panels agree well with their corresponding experimental values, and the maximum difference between the two values is found to be 10.3% for the 12.32 mm thick flat plate. Salient findings of the work are summarized below.

- For quasi-static indentation of curved panels, the initial stiffness (slope of the indentation force versus the indentation

depth curve) of a panel increases with a decrease in the magnitude of the radius of curvature irrespective of the sign of the curvature. For a fixed value of the radius of curvature, the initial stiffness increases with an increase in the plate thickness.

- For large indentations of thin panels, the tangent stiffness of a panel with the positive curvature is much smaller than that of the same panel with the negative curvature. For thicker plates, however, the sign of the curvature does not affect the tangent stiffness.
- For flat plates impacted at 30 m/s, the time when the impactor finally separates from the plate monotonically decreases with an increase in the plate thickness and is close to the time

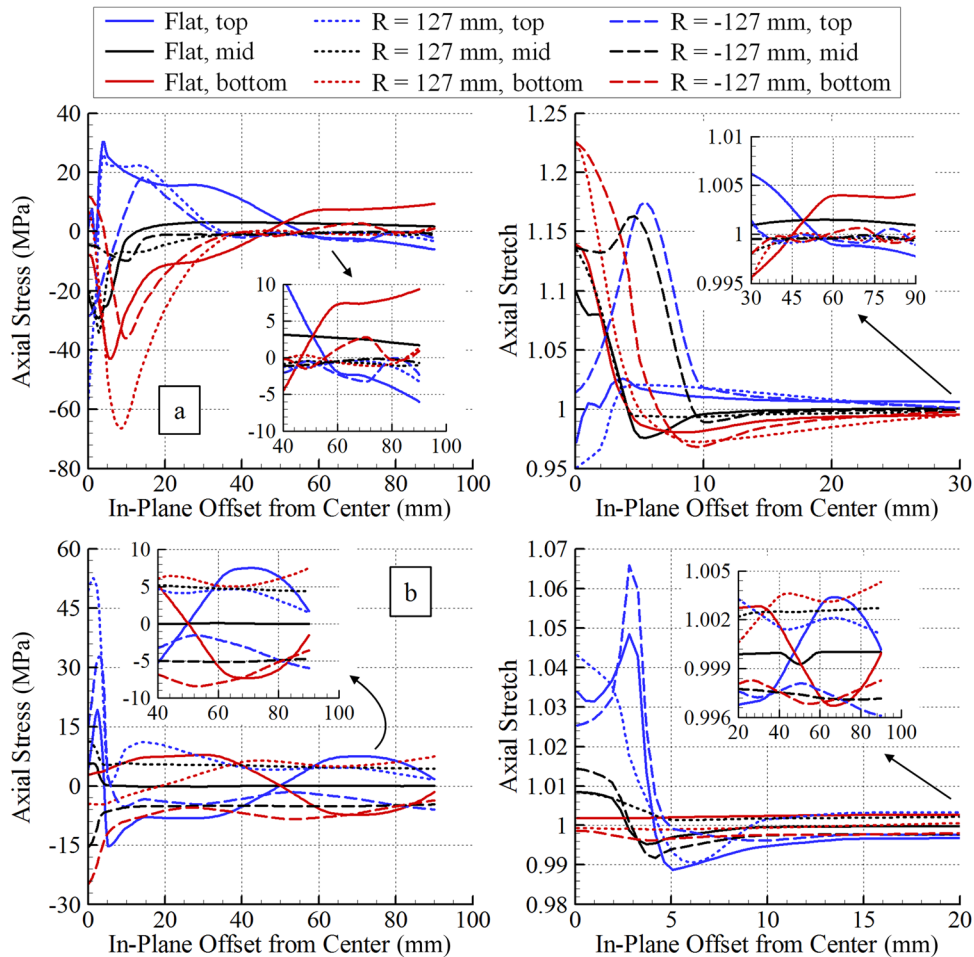


**Fig. 25** Axial stress and axial stretch as a function of the distance from the plate center at the top, midplane, and bottom of the (a) 3.00 mm and (b) 12.32 mm thick plates for 50 m/s impact speed when the impactor separates from the plate

when panels revert back to the position of zero central deflection. The maximum effective plastic strain occurs near the top surface for the 3 mm thick panel but near the bottom surface for the 12.32 mm thick panel, and the former equals about three times the latter. The 3 mm thick panel has regions

of positive and negative curvature but the 12.32 mm thick panel is essentially flat. For the 12.32 mm thick plate, the impactor bounces from the plate and then re-establishes contact before the eventual separation. However, no such rebounding occurs for the 3 mm thick plate. There is no

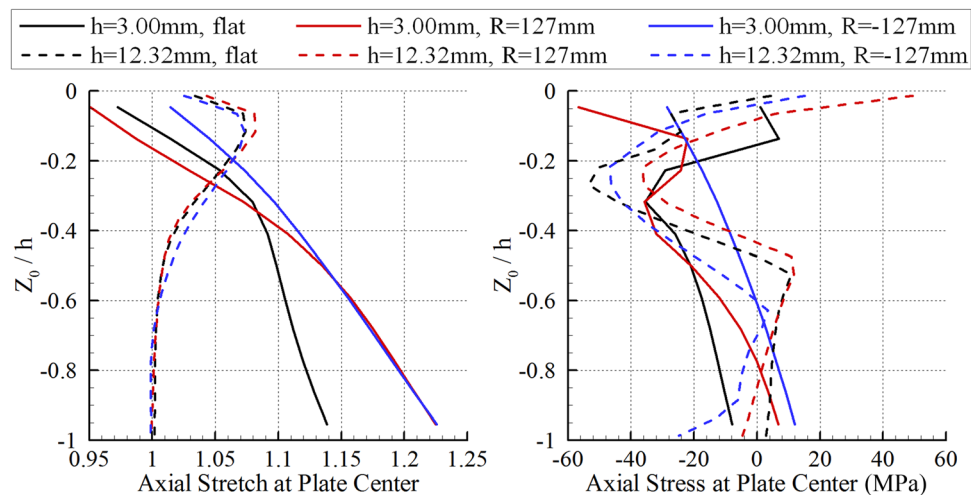


**Fig. 26** Through the thickness variations of the axial stretch and the axial stress on the transverse normal passing through the plate centroid for 20 m/s impact velocity at the time when the impactor separates from the plate

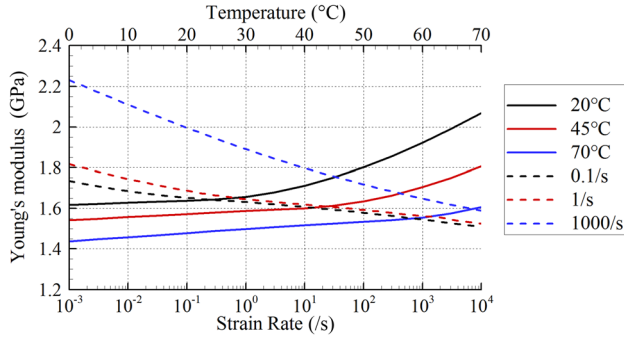


**Fig. 27** Variation with the strain rate and temperature of the total Young's modulus ( $E_\alpha + E_\beta$ ) of the PC

“neutral surface” for the 9.27 and the 12.32 mm thick plates and that for the 3, 4.42, and 9.27 mm thick plates is close to their top surface. Here, the “neutral surface” is defined as one infinitesimal lines on which are not stretched during plate's deformations.

- When the 5.85 mm thick flat plate impacted at 10, 20, 30, 40, and 50 m/s by the 104 g rigid hemispherical-nosed circular cylinder reverts back to the configuration of zero centroidal deflection, the effective plastic strain induced is maximum at a point on the top surface for the 10 m/s impact speed but at a point on the bottom surface for the other impact speeds. The qualitative nature of other deformation measures is unaffected by the impact speeds considered.
- The axial stress developed near the center of a negatively curved panel is positive and larger in magnitude than the axial stress in panels with  $R > 0$ . However, this statement does not hold for the 12.32 mm thick panels.
- For the 20 m/s impact speed and 3 mm thick panels of negative curvature, the impact performance of a panel decreases with an increase in the magnitude of curvature and the maximum effective plastic strain developed in the material is larger than that in the corresponding flat plate. However, no such correlation could be found for panel of positive curvature. For the 12.32 mm thick panels of both positive and negative curvatures, the maximum effective plastic strains induced near the center of the panel decrease with an increase in the magnitude of curvature.
- Bending deformations become more important relative to in-plane stretching/compression of the panels with an increase in the panel thickness. The panel thickness at which the transition from stretching dominance to bending dominance occurs is left for a future study. For thick panels, the maximum effective plastic strain occurs at a point away from the impacted surface irrespective of the panel curvature whereas for a thin panel it is at a point either on the top or the bottom surface.

## Acknowledgment

This research was sponsored by the Army Research Laboratory and was accomplished under Cooperative Agreement No. W911NF-06-2-0014. The views and conclusions contained in this document are those of the authors and should not be interpreted as representing the official policies, either expressed or implied, of the Army Research Laboratory or the U.S. Government. The U.S. Government is authorized to reproduce and distribute reprints for Government purposes notwithstanding any copyright notation hereon.

## Appendix A: Material Model for the PC

We assume that the total Cauchy stress tensor  $\sigma$  at a material point equals the sum of contributions from three phases, namely B,  $\alpha$ , and  $\beta$ , i.e.,  $\sigma = \sigma_B + \sigma_\alpha + \sigma_\beta$ . The three phases coexist at a

material point and have the same value of the deformation gradient  $\mathbf{F}$ . The phase B behaves like a nonlinear elastic Langevin spring for which

$$\sigma_B = \frac{C_R \sqrt{N_l}}{3} \frac{\lambda^p}{\lambda^p} L^{-1} \left( \frac{\lambda^p}{\sqrt{N_l}} \right) \bar{\mathbf{B}}_B \quad (\text{A1})$$

Here,  $\sigma_B$  is the Cauchy stress tensor,  $\bar{\mathbf{B}}_B$  is the deviatoric part of  $\bar{\mathbf{B}}_B = (J)^{-2/3} \mathbf{F} \mathbf{F}^T$ ,  $\lambda^p = \sqrt{\text{tr}(\bar{\mathbf{B}}_B/3)}$  is a measure of stretch,  $\text{tr}(\cdot)$  is the trace operator,  $L^{-1}$  is the inverse of the Langevin function defined by  $L(\beta) \equiv \coth \beta - 1/\beta$ ,  $N_l$  is the limiting stretch,  $C_R \equiv n_R k \theta$  is the rubbery modulus,  $\theta$  is the temperature in Kelvin,  $k$  is the Boltzmann's constant, and  $n_R$  is a material parameter.

The other two phases,  $\alpha$  and  $\beta$ , are modeled with the same constitutive equation but with different values of material parameters. For each phase, the deformation gradient  $\mathbf{F}$  is decomposed into elastic and plastic parts, e.g., see Refs. [36,37].

$$\mathbf{F} = \mathbf{F}_\alpha^e \mathbf{F}_\alpha^p, \quad \mathbf{F} = \mathbf{F}_\beta^e \mathbf{F}_\beta^p \quad (\text{A2})$$

Neither  $\mathbf{F}_\alpha^e$ ,  $\mathbf{F}_\beta^e$  nor  $\mathbf{F}_\alpha^p$ ,  $\mathbf{F}_\beta^p$  is gradient of a vector field. The plastic deformation gradients  $\mathbf{F}_\alpha^p$  and  $\mathbf{F}_\beta^p$  map a material point in the reference configuration to a material point in the intermediate configuration obtained after elastically unloading the current configuration to a stress-free state.

The rate of the plastic deformation gradient in phases  $\alpha$  and  $\beta$  is given by

$$\dot{\mathbf{F}}_\alpha^p = \mathbf{F}_\alpha^{e-1} \tilde{\mathbf{D}}_\alpha^p \mathbf{F}, \quad \dot{\mathbf{F}}_\beta^p = \mathbf{F}_\beta^{e-1} \tilde{\mathbf{D}}_\beta^p \mathbf{F} \quad (\text{A3})$$

where  $\tilde{\mathbf{D}}_i^p$  is the plastic strain-rate tensor in phase  $i$  ( $i = \alpha, \beta$ ) and it has been assumed that the plastic spin tensors in phases  $\alpha$  and  $\beta$  identically vanish. We note that  $\tilde{\mathbf{D}}_i^p$  does not equal the symmetric part of the velocity gradient (with respect of  $\mathbf{x}$ ) of phase  $i$ .

The Hencky elastic strain tensors of phases  $\alpha$  and  $\beta$  are defined as

$$\epsilon_\alpha^e = \ln \left( \sqrt{\mathbf{F}_\alpha^e \mathbf{F}_\alpha^{eT}} \right), \quad \epsilon_\beta^e = \ln \left( \sqrt{\mathbf{F}_\beta^e \mathbf{F}_\beta^{eT}} \right) \quad (\text{A4})$$

and the corresponding Cauchy stress tensors are given by

$$\sigma_\alpha = \frac{1}{J} [2\mu_\alpha \epsilon_\alpha^e + \lambda_\alpha \text{tr}(\epsilon_\alpha^e) \delta], \quad (\text{A5})$$

$$\sigma_\beta = \frac{1}{J} [2\mu_\beta \epsilon_\beta^e + \lambda_\beta \text{tr}(\epsilon_\beta^e) \delta]$$

where Young's moduli of phases  $\alpha$  and  $\beta$  of PC and consequently Lamé's constants,  $\lambda$  and  $\mu$ , are temperature and strain-rate dependent. They partly capture the temperature and the strain-rate dependence of the material response while Poisson's ratio is taken to be constant. Using test data given in the Appendix of Mulliken's thesis [6], we compute the temperature and the strain-rate dependence of Young's moduli of PC. These results are depicted in Fig. 27 and imply that the total Young's modulus increases with an increase in the strain rate and decreases with a rise in the temperature.

We note that Eq. (A5) is valid for finite deformations and accounts for all geometric nonlinearities.

The plastic strain rates are assumed to be coaxial with the deviatoric Cauchy stress tensors in their respective phases, that is

$$\tilde{\mathbf{D}}_\alpha^p = \dot{\gamma}_\alpha^p \frac{\sigma'_\alpha}{|\sigma'_\alpha|}, \quad \tilde{\mathbf{D}}_\beta^p = \dot{\gamma}_\beta^p \frac{\sigma'_\beta}{|\sigma'_\beta|} \quad (\text{A6})$$

where  $\sigma'_i$  ( $i = \alpha, \beta$ ) is the deviatoric part of the Cauchy stress in phase  $i$ ,  $|\sigma'_i| = \sqrt{\text{tr}(\sigma'_i \sigma'_i)}$  is the magnitude of  $\sigma'_i$ , and  $\dot{\gamma}_i^p$  is the effective plastic strain rate in phase  $i$ . This equation implies that  $\text{tr}(\tilde{\mathbf{D}}_i^p) = 0$ .

The effective plastic strain rates in  $\alpha$  and  $\beta$  phases are given by

$$\dot{\gamma}_i^p = \dot{\gamma}_{0i}^p \exp \left[ -\frac{\Delta G_i}{k\theta} \left( 1 - \frac{\tau_i}{t_i \hat{s}_i + \alpha_i^p p} \right) \right], \quad i = \alpha, \beta \quad (\text{A7})$$

where  $\dot{\gamma}_{0i}^p$  ( $i = \alpha, \beta$ ) is the pre-exponential factor,  $\Delta G_i$  is the activation energy,  $p = -\text{tr}(\boldsymbol{\sigma})/3$  is the pressure,  $\tau_i = \sqrt{0.5(\boldsymbol{\sigma}'_i \boldsymbol{\sigma}'_i)}$  is the effective stress,  $\alpha_i^p$  is the pressure coefficient,  $\hat{s}_i = 0.077\mu_i/(1 - \nu_i)$  is the athermal shear strength,  $\nu_i$  is the Poisson's ratio,  $k$  is the Boltzmann's constant, and  $t_i$  is an internal variable that evolves with plastic deformations. The variable  $\hat{s}_i$  is function of  $\mu_i$  and is, therefore, temperature and strain-rate dependent. Since no yield surface is postulated, plastic deformations always occur. The evolution of internal variable  $t_i$  in phases  $\alpha$  and  $\beta$  is given by

$$\dot{t}_i = \frac{h_i}{\hat{s}_i^0} \left( 1 - \frac{t_i}{t_i^{ss}} \right) \dot{\gamma}_i^p, \quad i = \alpha, \beta \quad (\text{A8})$$

where  $t_i^{ss}$  and  $h_i$  are softening parameters, and  $\hat{s}_i^0$  is the reference value of  $\hat{s}_i$  given by the reference values of  $\mu_i$  and  $\nu_i$ . Equation (A5) implies that the internal variable  $t_i$  remains constant for elastic deformations.

We postulate that the energy dissipated during plastic deformations in the  $\alpha$  and  $\beta$  phases is converted into heat, that is,

$$\dot{Q} = J \cdot (\boldsymbol{\sigma}_\alpha : \dot{\mathbf{D}}_\alpha^p + \boldsymbol{\sigma}_\beta : \dot{\mathbf{D}}_\beta^p) \quad (\text{A9})$$

where  $\dot{Q}$  is the heat generated per unit volume in the reference configuration. It is assumed that heating is mostly adiabatic for the impact problems studied here because there is no enough time for the heat to be conducted away, and neglecting heat conduction facilitates numerical integration of the governing differential equations. Thus, the temperature rise is given by Eq. (1)<sub>4</sub>. We note that  $\dot{Q} \neq \tau_\alpha \dot{\gamma}_\alpha^p + \tau_\beta \dot{\gamma}_\beta^p$ . In metal plasticity, the equality holds in this expression but there are no different phases.

We refer the reader to Mulliken's thesis [6], Mulliken and Boyce [5] and Varghese and Batra [18] for the determination of values of material parameters from the test data for the PC,

**Table 3 Values of material parameters for the PC**

	Phase $\alpha$	Phase $\beta$	Phase B	Common
$\nu_i$	0.38	0.38		
$\dot{\gamma}_{0i}^p$ (/s)	$2.94 \times 10^{16}$	$3.39 \times 10^5$		
$\Delta G_i$ (J)	$3.744 \times 10^{-19}$	$3.769 \times 10^{-20}$		
$\alpha_i^p$	0.168	0.245		
$h_i$ (Mpa)	125	400		
$t_i^{ss}$	0.33	2.00		
$C_R$ at 300 K (Mpa)			35.0	
$N_i$			12.25	
$c$ (J/(g·K))				1.20
$\rho$ (g/cm <sup>3</sup> )				1.20
$E$ (Gpa) at 300 K, 5000/s	1.678	0.344		

which are given in Table 3 and for the comparison of the computed and experimental axial stress versus axial strain curves.

## Appendix B: FE Mesh

An example with a very coarse mesh is shown in Fig. 28 with dimensions of specimens used in experiments conducted by Gunnarsson et al. [31–33].

The pattern of the FE mesh in the  $xy$ -plane is obtained by partitioning the plate along its diagonals. Then, each of the four quarters of the plate is partitioned by a 12.7-mm radius circle centered at the point of impact. Each quarter of the circumference of the circle, the part of each one of the four diagonals that are within the circle, and each edge of the plate are discretized with 38 uniform elements. The outer part of the plate diagonals, i.e., the part located more than 12.7-mm from the plate center, is divided into 48 segments of different lengths so that the ratio of the length of the smallest segment—located near the circle—to that of the largest segment—located at the corner—equals 20. Each layer has 11,628 elements, and 11, 15, 18, 29, and 39 layers are used for the 3.0-mm, 4.45-mm, 5.85-mm, 9.27-mm, and 12.32-mm thick PC plates, respectively.

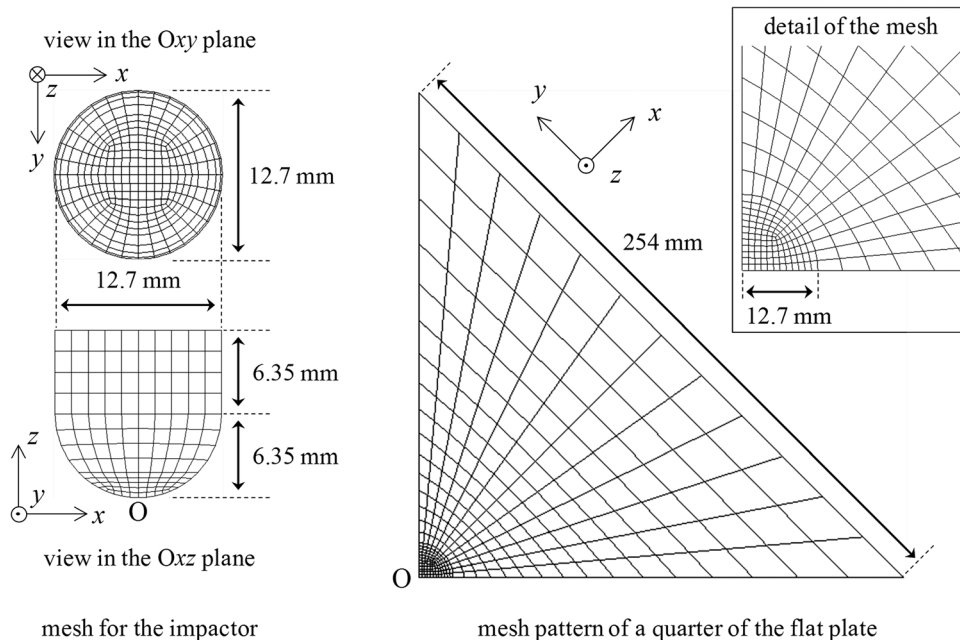


**Fig. 28 Coarse mesh for the impactor and the square plate (much finer meshes were used for the simulations)**

The FE mesh for the impactor near the contact region was refined until the element size there was comparable to that of elements at the plate center. The rest of the impactor was discretized with a coarse mesh. The FE mesh for the impactor has 8576 elements.

## References

- [1] Radin, J., and Goldsmith, W., 1988, "Normal Projectile Penetration and Perforation of Layered Targets," *Int. J. Impact Eng.*, **7**(2), pp. 229–259.
- [2] Sands, J., Patel, P., Dehmer, P., and Hsieh, A., 2004, "Protecting the Future Force: Transparent Materials Safeguard the Army's Vision," *AMPTIAC Q.*, **8**(4), pp. 28–36.
- [3] Siviour, C. R., Walley, S. M., Proud, W. G., and Field, J. E., 2005, "The High Strain Rate Compressive Behaviour of Polycarbonate and Polyvinylidene Difluoride," *Polymer*, **46**(26), pp. 12546–12555.
- [4] Moy, P., Weerasooriya, T., Hsieh, A., and Chen, W., 2003, "Strain Rate Response of a Polycarbonate Under Uniaxial Compression," SEM Conference on Experimental Mechanics, Charlotte, NC, June 2–4, Society for Experimental Mechanics, Bethel, CT, pp. 2–4.
- [5] Mulliken, A. D., and Boyce, M. C., 2006, "Mechanics of the Rate-Dependent Elastic-Plastic Deformation of Glassy Polymers From Low to High Strain Rates," *Int. J. Solids Struct.*, **43**(5), pp. 1331–1356.
- [6] Mulliken, A. D., 2006, "Mechanics of Amorphous Polymers and Polymer Nanocomposites During High Rate Deformation," Ph.D. thesis, Massachusetts Institute of Technology, Cambridge, MA.
- [7] Richeton, J., Ahzi, S., Daridon, L., and Remond, Y., 2005, "A Formulation of the Cooperative Model for the Yield Stress of Amorphous Polymers for a Wide Range of Strain Rates and Temperatures," *Polymer*, **46**(16), pp. 6035–6043.
- [8] Richeton, J., Schlatter, G., Vecchio, K. S., Remond, Y., and Ahzi, S., 2005, "A Unified Model for Stiffness Modulus of Amorphous Polymers Across Transition Temperatures and Strain Rates," *Polymer*, **46**(19), pp. 8194–8201.
- [9] Richeton, J., Ahzi, S., Vecchio, K. S., Jiang, F. C., and Adharapurapu, R. R., 2006, "Influence of Temperature and Strain Rate on the Mechanical Behavior of Three Amorphous Polymers: Characterization and Modeling of the Compressive Yield Stress," *Int. J. Solids Struct.*, **43**(7–8), pp. 2318–2335.
- [10] Fleck, N. A., Stronge, W. J., and Liu, J. H., 1990, "High Strain-Rate Shear Response of Polycarbonate and Polymethyl Methacrylate," *Proc. R. Soc. London, Ser. A*, **429**(1877), pp. 459–479.
- [11] Ramakrishnan, K. R., 2009, "Low Velocity Impact Behaviour of Unreinforced Bi-Layer Plastic Laminates," Doctoral dissertation, Australian Defence Force Academy, Canberra, Australia.
- [12] Rittel, D., 2000, "An Investigation of the Heat Generated During Cyclic Loading of Two Glassy Polymers. Part I: Experimental," *Mech. Mater.*, **32**(3), pp. 131–147.
- [13] Rittel, D., and Rabin, Y., 2000, "An Investigation of the Heat Generated During Cyclic Loading of Two Glassy Polymers. Part II: Thermal Analysis," *Mech. Mater.*, **32**(3), pp. 149–159.
- [14] Rittel, D., 1999, "On the Conversion of Plastic Work to Heat During High Strain Rate Deformation of Glassy Polymers," *Mech. Mater.*, **31**(2), pp. 131–139.
- [15] Richeton, J., Ahzi, S., Vecchio, K. S., Jiang, F. C., and Makradi, A., 2007, "Modeling and Validation of the Large Deformation Inelastic Response of Amorphous Polymers Over a Wide Range of Temperatures and Strain Rates," *Int. J. Solids Struct.*, **44**(24), pp. 7938–7954.
- [16] Tervoort, T., Smit, R., Brekelmans, W., and Govaert, L. E., 1997, "A Constitutive Equation for the Elasto-Viscoplastic Deformation of Glassy Polymers," *Mech. Time-Depend. Mater.*, **1**(3), pp. 269–291.
- [17] Boyce, M. C., Parks, D. M., and Argon, A. S., 1988, "Large Inelastic Deformation of Glassy-Polymers. Part I. Rate Dependent Constitutive Model," *Mech. Mater.*, **7**(1), pp. 15–33.
- [18] Varghese, A. G., and Batra, R. C., 2009, "Constitutive Equations for Thermo-mechanical Deformations of Glassy Polymers," *Int. J. Solids Struct.*, **46**(22–23), pp. 4079–4094.
- [19] Varghese, A. G., and Batra, R. C., 2011, "Strain Localization in Polycarbonates Deformed at High Strain Rates," *J. Polym. Eng.*, **31**(6–7), pp. 495–519.
- [20] Safari, K. H., Zamani, J., Ferreira, F. J., and Guedes, R. M., 2013, "Constitutive Modeling of Polycarbonate During High Strain Rate Deformation," *Polym. Eng. Sci.*, **53**(4), pp. 752–761.
- [21] Shen, J. H., Lu, G. X., Wang, Z. H., and Zhao, L. M., 2010, "Experiments on Curved Sandwich Panels Under Blast Loading," *Int. J. Impact Eng.*, **37**(9), pp. 960–970.
- [22] Jing, L., Wang, Z., Shim, V., and Zhao, L., 2014, "An Experimental Study of the Dynamic Response of Cylindrical Sandwich Shells With Metallic Foam Cores Subjected to Blast Loading," *Int. J. Impact Eng.*, **71**, pp. 60–72.
- [23] Kim, S. J., Goo, N. S., and Kim, T. W., 1997, "The Effect of Curvature on the Dynamic Response and Impact-Induced Damage in Composite Laminates," *Compos. Sci. Technol.*, **57**(7), pp. 763–773.
- [24] Ramkumar, R. L., and Thakar, Y. R., 1987, "Dynamic-Response of Curved Laminated Plates Subjected to Low Velocity Impact," *J. Eng. Mater.*, **109**(1), pp. 67–71.
- [25] Khalili, S. M. R., and Ardali, A., 2013, "Low-Velocity Impact Response of Doubly Curved Symmetric Cross-Ply Laminated Panel With Embedded SMA Wires," *Compos. Struct.*, **105**, pp. 216–226.
- [26] Her, S. C., and Liang, Y. C., 2004, "The Finite Element Analysis of Composite Laminates and Shell Structures Subjected to Low Velocity Impact," *Compos. Struct.*, **66**(1–4), pp. 277–285.
- [27] Lin, H. J., and Lee, Y. J., 1990, "On the Inelastic Impact of Composite Laminated Plate and Shell Structures," *Compos. Struct.*, **14**(2), pp. 89–111.
- [28] Leylek, Z., Scott, M. L., Georgiadis, S., and Thomson, R. S., 1999, "Computer Modelling of Impact on Curved Fibre Composite Panels," *Compos. Struct.*, **47**(1–4), pp. 789–796.
- [29] Khalili, S. M. R., Soroush, M., Davar, A., and Rahmani, O., 2011, "Finite Element Modeling of Low-Velocity Impact on Laminated Composite Plates and Cylindrical Shells," *Compos. Struct.*, **93**(5), pp. 1363–1375.
- [30] Batra, R. C., and Gobinath, T., 1991, "Steady State Axisymmetric Deformations of a Thermoviscoplastic Rod Penetrating a Thick Thermoviscoplastic Target," *Int. J. Impact Eng.*, **11**(1), pp. 1–31.
- [31] Gunnarsson, C. A., Weerasooriya, T., and Moy, P., 2008, "Measurement of Transient Full-Field, Out-of-Plane Back Surface Displacements of Polycarbonate During Impact," 11th International Congress & Exposition on Experimental & Applied Mechanics, Orlando, FL, June 2–5, pp. 1403–1413.
- [32] Gunnarsson, C. A., Weerasooriya, T., and Moy, P., 2011, "Impact Response of PC/PMMA Composites," *Dynamic Behavior of Materials*, Vol. 1, Springer, New York, pp. 195–209.
- [33] Gunnarsson, C. A., Ziemski, B., Weerasooriya, T., and Moy, P., 2009, "Deformation and Failure of Polycarbonate During Impact as a Function of Thickness," International Congress and Exposition on Experimental Mechanics and Applied Mechanics, Society for Experimental Mechanics, Albuquerque, NM, June 1–4.
- [34] Chen, X. J., and Batra, R. C., 1995, "Deep Penetration of Thick Thermoviscoplastic Targets by Long Rigid Rods," *Comput. Struct.*, **54**(4), pp. 655–670.
- [35] Antoine, G. O., and Batra, R. C., 2014, "Sensitivity Analysis of Low-Velocity Impact Response of Laminated Plates," *Int. J. Impact Eng.*, **78**, pp. 64–80.
- [36] Kröner, E., 1959, "Allgemeine kontinuumstheorie der versetzungen und eigenspannungen," *Arch. Ration. Mech. Anal.*, **4**(1), pp. 273–334.
- [37] Lee, E. H., 1969, "Elastic-Plastic Deformation at Finite Strains," *ASME J. Appl. Mech.*, **36**(1), pp. 1–6.